공학박사학위논문

Multifunctional Surface-enhanced Raman Scattering Nanoprobe and Encoding Materials for Ligand Screening

다기능성 표면 증강 라만 산란 나노프로브 및

리간드 스크리닝을 위한

인코딩 물질의 개발에 관한 연구

2017년 8월

서울대학교 대학원

화학생물공학부

정 철 환

Multifunctional Surface-enhanced Raman Scattering Nanoprobe and Encoding Materials for Ligand Screening

다기능성 표면 증강 라만 산란 나노프로브 및
리간드 스크리닝을 위한 인코딩 물질의 개발에 관한 연구

지도 교수 이 윤 식

이 논문을 공학박사학위논문으로 제출함
2017년 8월
서울대학교 대학원
화학생물공학부
정 철 환

정철환의 공학박사학위논문을 인준함
2017년 7월

위 원 장 장 정 식 (인)

부위원장 이 윤 식 (인)

위 원 황 석 연 (인)

위 원 정 대 홍 (인)

위 원 전 봉 현 (인)

ABSTRACT

Multifunctional Surface-enhanced Raman Scattering Nanoprobe and Encoding Materials for Ligand Screening

Cheolhwan Jeong

School of Chemical and Biological Engineering

The Graduate School

Seoul National University

Surface-enhanced Raman scattering (SERS) has been widely utilized in bio applications due to its great advantages in multiplex detection. By controlling the structure of SERS active materials, effective SERS nanoprobes have been developed with additional functionality and strong SERS signals.

In chapter 1, the fabrication of multilayered tri-functional magnetic-fluorescence-SERS nanoprobes (MF-SERS dots) containing superparamagnetic Fe_3O_4 nanoparticles (NPs) clusters, assembled Ag NPs, and fluorescent silica layer is described. The MF-SERS dots exhibite both superparamagnetism and fluorescence properties, and can

also generate strong SERS signals from the assembled Ag NPs after treating four kinds of Raman reporter molecules; 4-fluorobenzenethiol (4-FBT), 4-chlorobenzenethiol (4-CBT), 4-bromobenzenethiol (4-BBT), and 3,4-dichlorobenzenethiol (3,4-DCT). The MF–SERS dots were internalized into cells, allowing successful separation of cells using an external magnetic field, and SERS and fluorescence signals were successfully detected from the NPs-containing cells. Also, CD44 antibody-conjugated MF-SERS dots were selectively bound to MDA-MB-231 cells. These results prove that MF-SERS dots are useful nanoprobes for multiplex detection and separation of cells.

In chapter 2, the application of silica based disk type encoding material (micro-encoder) using graphical patterns and SERS signal is presented. The size and thickness of micro-encoders is 5 μm and 1 μm respectively, and 1 μm-sized holes are located on the micro-encoders. Each encoders can be distinguished by the number of holes and characteristic SERS signals of three kinds of Raman reporter molecules (4-FBT, 4-CBT, and 4-BBT) from the assembled Ag NPs on the micro-encoders. During solid-phase peptoid synthesis, the peptoid side chain can be encoded by the absorption of micro-encoders on the bead which is 100 μm in size. And the sequence and the type of peptoid side chain can be decoded with the number of holes in each micro-encoder and the SERS signals, respectively. The amount of absorbed micro-encoders on bead is

dependent on the amount of treated micro-encoders, and for practical application, 10% of treated micro-encoders were introduced on the bead. The conditions of peptoid coupling reaction are optimized for maintaining appropriate amount of micro-encoders on the bead during peptoid synthesis. Thus, the appropriate amounts of bromoacetic acid and primary amine are determined to be 10 equivalent of the amine functional groups on the bead. Finally, the pepoid sequences, which are composed of 2-methoxyethylamine (N_{mea}), *N*-(3-aminopropyl)-2-pyrrolidinone (N_{app}), 1-naphtylmethylamine (N_{nap}), piperonylamine (N_{pip}), and isobutylamine (N_{leu}), are synthesized, and the last three sequences are encoded using the micro-encoders. Then, the streptavidin bound beads are analyzed by the graphical pattern and the SERS signals of the micro-encoders on the beads, as a decoding process, which can effectively provide the information about the peptoid sequence. These results prove that the graphical and SERS dual modal micro-encoders can be utilized as an effective agent for screening of peptoid as well as small molecule ligands on bead by simple encoding-decoding processess.

Keywords: Surface-enhanced Raman scattering, Multifunctional nanoparticles, Superparamagnetic nanoparticles, Cell separation, Multiplex detection, Bio-imaging, Peptoid, Optical encoding, Peptoid encoding, Graphical encoding, Ligand screening

Student number: 2013-20997

TABLE OF CONTENTS

LIST OF TABLES

LIST OF FIGURES

LIST OF ABBREVIATIONS

3,4-DCT	3,4-Dichlorothiophenol
4-BBT	4-Bromobenzenethiol
4-CBT	4-Chlorobenzenethiol
4-FBT	4-Fluorothiophenol
6MP	6-Mercaptopurine
APTS	3-Aminopropyltriethoxysilane
Ag-M-silica NPs	Ag NPs assembled M-Silica NPs
BOP	(Benzotriazol-1-yloxy)tris(dimethylamino)phosphonium hexafluorophosphate
DIC	*N*,*N*´-diisopropylcarbodiimide
DIEA	*N*,*N*-diisopropylethylamine
DMAP	4-(Dimethylamino)pyridine
DMEM	Dulbecco's modified Eagle's medium
DMF	*N*,*N*-dimethylformamide
EDX	Energy dispersive X-ray spectroscopy
EG	Ethylene glycol
ESI-MS	Electrospray ionization mass spectrometry
EtOH	Hydroxybenzotriazole
FACS	Fluorescence-activated cell sorting
FBS	Fetal bovine serum
Fmoc	9-Fluorenylmethoxycarbonyl
FWHM	Full width at half maximum
HBTU	2-(1*H*-benzotriazole-1-yl)-1,1,3,3-tetramethyluronium hexafluorophosphate
$HOBt_4$	Hydroxybenzotriazole
IPA	Isopropylalcohol
MC	Methylene chloride
MF-SERS dots	Magnetic-fluorescence SERS nanparticles
Micro-encoders	Silica-coated Ag NPs-assembled micro-disks

MMI	Methimazole
MPTS	3-Mercaptopropyltrimethoxysilane
M-silica NPs	Magnetic-silica NPs
NHS	*N*-hydroxysuccinimide
NIR	Near-infrared
NMP	*N*-methyl-2-pyrrolidone
NPs	Nanoparticles
N_{app}	*N*-(3-aminopropyl)-2-pyrrolidinone
N_{leu}	Isobutylamine
N_{mea}	2-Methoxyethylamine
N_{nap}	1-Naphtylmethylamine
N_{pip}	Piperonylamine
PBS	Phosphate buffered saline
PLL	Photolabile linker
PVP	Polyvinylpyrrolidone
QD	Quantum dot
RITC	Rhodamine B isothiocyanate
SEM	Scanning electron microscope
SERRS	Surface-enhanced resonance Raman scattering
SERS	Surface-enhanced Raman scattering
SERS dots	Ag NPs-assembled silica NPs
Streptavidin-FITC	Streptavidin-conjugated fluorescein isothiocyanate
TEM	Transmission electron microscope
TEOS	Tetraethyl orthosilicate
TG beads	TentaGel beads
TMAH	Tetrametylammonium hydroxide

Multifunctional Surface-enhanced Raman Scattering Nanoprobe and Encoding Materials for Ligand Screening

Introduction

1. Surface-enhanced Raman Scattering

1.1. Advantages of Surface-Enhanced Raman Scattering in Bioapplications

Raman spectroscopy is a promising optical detection technique that can be utilized to obtain valuable information about molecular structures, conformation, and interactions based on the vibrational modes of a molecule. These characteristics of Raman spectroscopy are suitable for the detection of biological molecules and the imaging of cells and tissues. However, Raman scattering cross sections are known to be 10 orders of magnitude smaller than the absorption and fluorescence cross sections of typical molecules. Thus, the Raman scattering signal has not been fully applied for practical use since its discovery in the 1930s. The weak signal of Raman scattering, even under high laser power, should be enhanced to take a leading role in studying biological systems.

The low sensitivity of Raman scattering can be improved by an optical phenomenon called surface-enhanced Raman scattering (SERS), which is generated when the molecules are located on the surface of the novel metal nanoparticles (NPs) such as gold or

silver (Fig. 1). Fleischmann *et al*. discovered the SERS effect for the first time in 1973 [1]. They obtained spectra of calomel (Hg_2Cl_2) on a roughened mercury electrode, which gave an extraordinarily strong intensity. They extended their work to pyridine adsorbed on a roughened silver electrode, which showed spectra with even higher quality. Later, Jeanmaire *et al*. proposed that the increased intensity of the spectra was a result of the roughened surface, which induced an enhanced Raman signal[2]. After these reports were published, various new techniques using SERS were developed for a wide variety of applications.

With the support of current developments in nanotechnology, SERS has become a prominent tool in the biomedical field. Based on the intrinsic advantages of SERS, it can serve as an accurate, sensitive, and practical sensing platform for biomolecular detection. Various analytical methods including label-free and multiplex detection have been reported using SERS. Chan *et al.* reported on Ag NPs embedded in an ordered array of anodic aluminum oxide, which was fabricated by electrochemical plating[3]. The size and interparticle gaps of Ag NPs on an aluminum oxide

template were optimized to generate a strong SERS signal. Then, various biomolecules including DNA, water pollutants, and β-carotene in low concentrations could be detected in a reproducible manner. Lierop *et al.* detected DNAs using Ag NPs and dye labeled DNA strands[4]. The dye labeled DNA strand was designed to hybridize with the target DNA strand and generate a SERS signal from the dye molecules after absorption on the Ag NPs. By using this nanoprobe, the presence of a specific DNA sequence can be identified without time-consuming and complex handling steps. Furthermore, Yang *et al.* reported on the multiplex detection of drugs in living cells[5]. After Ag NPs were internalized into cells, SERS signals from 6-mercaptopurine (6MP) and methimazole (MMI) were obtained. The diffusion and metabolism of 6MP and MMI in a living cell could be monitored by analyzing the concentration variations of 6MP and MMI.

Two mechanisms are known to be related to the strong enhancement of a SERS signal. The localized surface plasmon resonance on the surface of noble metal[6, 7] can enhance the SERS signal by 10–11 orders of magnitude. In addition to this

electromagnetic mechanism, the chemisorption of molecules onto the surface of metal contributes to the SERS signal enhancement by 2–4 orders of magnitude by the interactions between electrons from the molecule and electrons from the metal surface[8, 9]. This largely enhanced signal enables Raman scattering to be used effectively for ultrasensitive and multiplex detection, especially in bio field. Another advantage of SERS for practical application is the linear dependency of SERS signals on the power of incident light. Although SERS has a nonlinear effect in signal enhancement, such a linear tendency of SERS signals to the power of incident light has a great advantage for the quantitative measurement of analytes. In addition, the SERS intensity could be changed by adjusting the wavelength of the incident laser lights. Since the resonance wavelength is determined by the surface plasmon of the metal nanostructure, the resonance conditions can be tuned by choosing the type of metals or by controlling their shapes[10-12]. Zheng *et al.* reported on core-satellite plasmonic nanostructures as sensitive SERS substrates at near-infrared (NIR) laser excitation[13]. The DNA-directed self-assembly resulted in the formation of core-

satellite Au NP structures and red shifted plasmon resonances. As expected, the nanostructures gave stronger SERS signals at NIR laser excitation compared with the excitation at a shorter wavelength. Likewise, the structure or shape of the metal can be designed and selected to control the resonance wavelength according to the purpose of the application, such as preventing the autofluorescence of biological materials or enhancing the penetration depth.

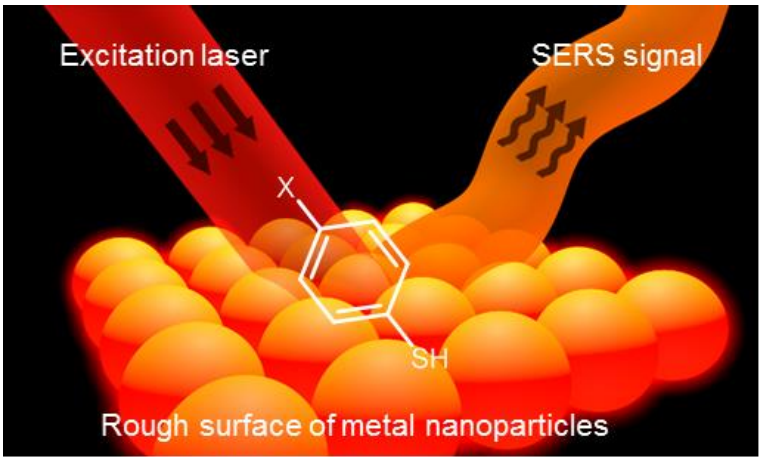

Figure 1. Schematic illustration for the enhanced Raman scattering signal when molecules are located on noble metal NPs.

1.2. SERS Active Nanostructures for Sensitive Detection

After the first report on SERS, there were an enormous number of reports on SERS active substrates, including various types of roughened structures[14] and metals such as gold, silver, copper, and aluminum. Many researchers made an effort to explain SERS enhancement and to find appropriate substrates that would cause huge enhancements in SERS intensity. In this regard, current studies are concentrating on the synthesis of controlled and reproducible metal nanostructures, which can generate so-called "hot spots." The "hot spots" are special areas around the metal surface that could lead to large enhancements of the SERS signal when molecules are properly located. Multidirectional approaches have been adopted to build up hot spots for the sensitive detection of molecules in a reproducible manner (Fig. 2). These include encapsulated silver NP aggregates[15], hollow-type gold NPs[16-18], nanorattles[19, 20], silver nanowire bundles[21, 22], gold NPs with thin oxide shells[23], polydimensional structure-like nanocubes[24, 25], dimeric nanospheres[26], gold nanocrescents[27], triangular NP arrays[28], flower-like gold NPs[29], star-shaped gold NPs[30], gold

nanorods[31-33], nanodisks[34], and gold nanorods immobilized on silica NPs[35].

Our group has reported on various types of Ag NP-assembled silica NPs (SERS dots)[36], which are composed of the following components: a silica core nanostructure for stable immobilization of metal NPs, metal NPs for the signal enhancement of Raman-active chemicals, Raman-active chemicals that exhibit a unique SERS vibrational signature, and further coating with silica to provide chemical and physical stability. The use of a silica nanostructure as a backbone for the immobilization of Ag NPs has many merits for the application of SERS dots. First, monodisperse silica NPs can be easily synthesized in desirable sizes, which makes the property of the resulting SERS dots controllable. Second, the silica backbone can act as a template to handle Ag NPs, as well as a domain for additional multifunctionality. In addition, the SERS dots generate strong SERS signals from the assembled Ag NPs with great reproducibility (Fig. 3). These key advantages enable SERS dots to be employed in various bioapplications effectively. Kang *et al.* utilized a highly sensitive and

biocompatible NIR-SERS probe for cell tracking in a live animal[37]. The thickness of the Ag shell and resonance plasmon wavelength of SERS dots were adjusted to obtain an NIR sensitive property and improve penetration depth. Thus, the SERS signal can be detected from NPs-containing A549 cells after subcutaneous injection of A549 cells into a nude mouse. Moreover, multifunctionalities were added to the SERS dots for various applications. Noh *et al.* reported on the detection and isolation of cells using magnetic SERS dots[38]. A magnetic core was added to the center of the SERS dots, and thus, the NPs were able to play an important role in the multiplex detection and rapid isolation of the desired cells. Woo *et al.* reported on the quantitative analysis of multiple proteins with fluorescent SERS dots[39]. Using the fluorescent property of the SERS dots, multiplex immunoassays for the detection of stem cells can be easily performed.

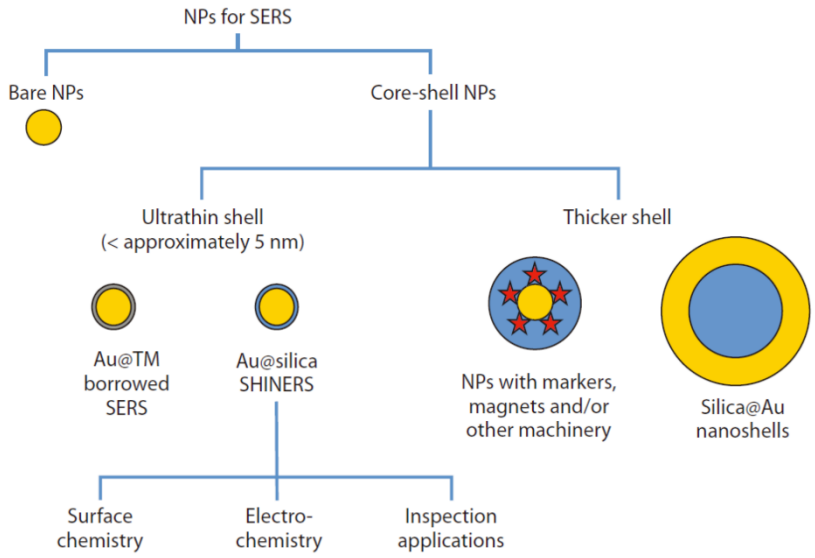

Figure 2. Various SERS active materials engineered for generating strong SERS signals[40].

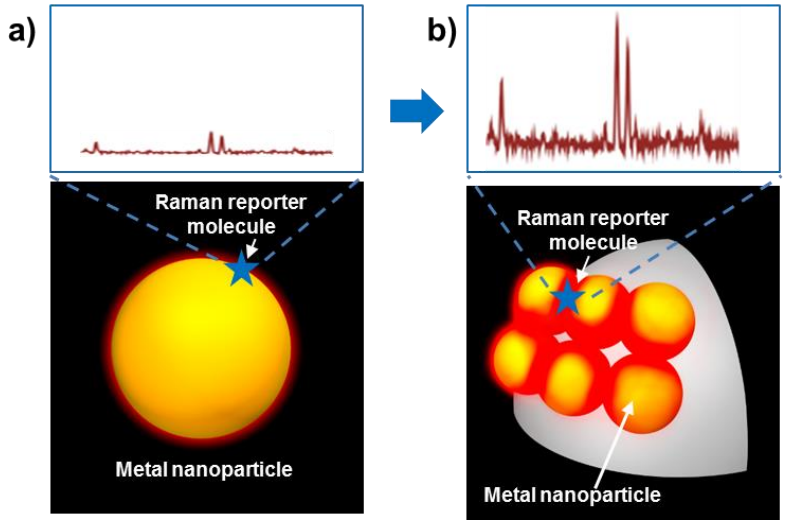

Figure 3. Schematic illustration of SERS active plasmonic NPs when a) existing as single NP and (b) assembled on backbone structure.

1.3. SERS Tagging Materials and Multiplex Detection

Detection methods using a SERS signal can be broadly divided into two categories: labeled and label free. In the label-free method, signals from the targets that are closely located on metal NPs are directly measured and analyzed without labeling. Because of the unique advantages of SERS techniques in real-time detection and the possibility of analyzing unknown samples, various target biomolecules such as DNA[41], proteins[42], viruses, and even small molecules[43] have been detected and analyzed using the label-free method. However, there have been many obstacles for the precise analysis of targets, including different signal intensities based on the structure of the target molecules, the excessive complexity of Raman signals, and a limited dynamic range.

In the labeled method, certain dye molecules are utilized as "Raman reporter molecules." The Raman reporter molecules generally have an aromatic structure that can generate simplified and strong SERS signals, and functional groups that have strong affinity for metal NPs. Because the Raman reporter molecules

generate less complicated and improved Raman signals compared with those of the label-free method, detecting the SERS peaks of the Raman reporter molecules can provide powerful advantages in multiplexing ability and sensitivity.

Such a SERS tagging method provides many advantages compared to other optical tagging methods. For example, fluorescence or fluorescent NPs have been exploited in various bioapplications[44], but they suffered from photobleaching during multiplexed detection or broad emission profiles that caused the overlap of emission bands. Semiconductor quantum dots (QDs) have attracted interest because they have narrower symmetrical emission peaks with minimal overlap between spectra[45, 46]. However, owing to significant drawbacks of QDs such as water incompatibility and potential toxicity, the broad application of QDs in biofield has been limited. In addition, the multiplexing capability of QDs is meaningless for *in vivo* applications because autofluorescence from tissue can also interfere with the emission peaks of QDs[47].

In this regard, the SERS technique has attracted great interest

owing to the superior features of SERS. First, SERS is not photo-bleachable. Second, SERS produces multiple molecular specific signals with a narrow bandwidth of full width at half maximum (FWHM) of less than 1 nm, which can prevent spectral overlap between various signals (Fig. 4). Third, the laser line can be chosen within a wide excitation wavelength range according to the SERS substrate. This can be very useful when the chemical resonance condition is needed for surface-enhanced resonance Raman scattering (SERRS) or to avoid the autofluorescence from a biological sample. In addition, the signal sensitivity can be augmented to the level of single-molecule detection when the SERS substrates are appropriately optimized [48, 49].

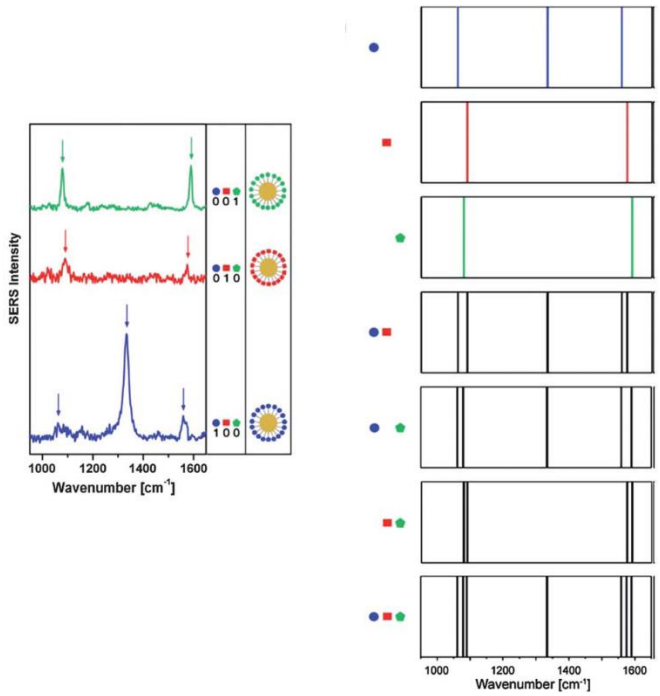

Figure 4. Molecular specific SERS spectra with narrow bandwidth, which can act as molecular fingerprint[50].

2. SERS Active Multifunctional Nanoprobes for Bioapplications

With a combination of other functionalities, multifunctional NPs have been considered as a promising material for the analysis of complicated biological systems[51]. As one of the modalities, the SERS property plays an active role in labeling multiple targets at the same time. Various types of multifunctional SERS active NPs have been reported, which are effective for the analysis of biological systems (Fig. 5)[52], such as identification and quantification of targets[53, 54], magnetic resonance imaging[55, 56], and photothermal therapy[57]. Such multifunctional NPs should be developed for the maximized utilization of their functions. In addition to the components of multifunctional NPs, the design of the structure of NPs is very important for their fabrication.

Superparamagnetic NPs have strong advantages in controlling the movement of NPs by an external magnetic field when utilized as an additional component of multifunctional NPs. A lack of remanence magnetization in the absence of an external magnetic

field is quite a significant property because it will prevent the agglomeration of NPs[58-60]. Superparamagnetic Fe_3O_4 NPs have been utilized as a basic tool for biomedical applications owing to their strong saturated magnetization, nontoxicity, and biocompatibility, in addition to their superparamagnetic nature. However, single Fe_3O_4 NP has limitations in practical application owing to its slow accumulation rate and low separation yield by an external magnet. Nanostructures having Fe_3O_4 NPs clusters on a silica core have been reported, which can overcome the drawbacks of single Fe_3O_4 NPs[61]. They afforded a more rapid accumulation rate than single Fe_3O_4 NPs, as well as complete separation under an external magnetic field, which is useful for cell separation.

Various dual-functional NPs having SERS and magnetic properties simultaneously have been reported. This can allow for the magnetic isolation and identification of targets at the same time[62, 63]. However, for practical use, SERS measurement still has room for improvement regarding the visualization and quantification of targets. Thus, trifunctional NPs that have magnetism, SERS, and fluorescence properties have been

developed. However, problems such as limitations on the availability of Raman reporter molecules that have strong SERS signals and remnant magnetization even after the elimination of the external magnetic field still remain[64, 65].

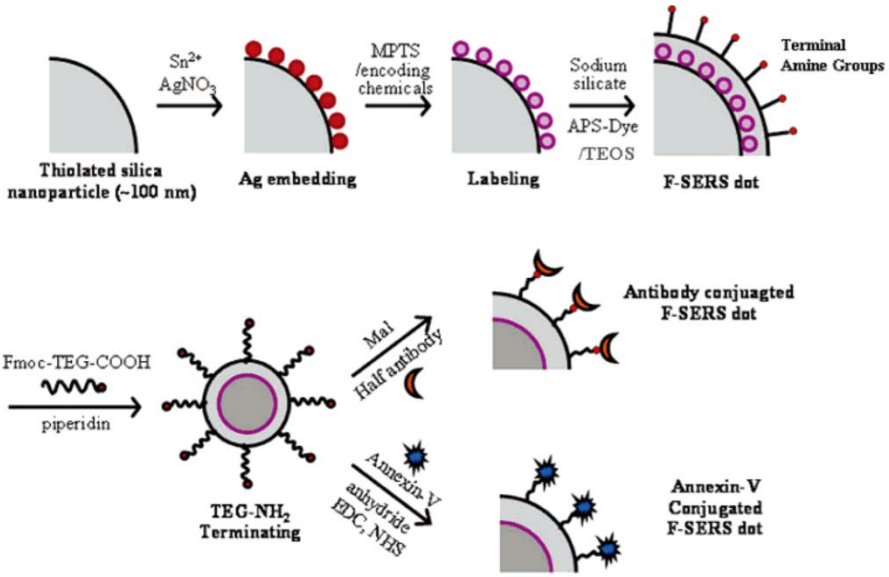

Figure 5. Schematic illustration of multiplex detection using SERS nanoprobes[52].

3. SERS Based Encoding Methods for Ligand Screening

Development of appropriate ligands such as peptides, nucleic acids, and peptoids that can bind to specific target molecule has attracted significant interest in the field of drug discovery[66, 67]. Among them, peptoids, which are poly-*N*-substituted glycines, have drawn much attention recently[68]. The biomimetic oligomers have a similar structure to peptides but are more resistant to protease degradation owing to the structural difference from the peptides having an achiral property (Fig. 6)[69]. Thus, peptoid can act as a useful peptide replacement that can recognize biomolecules, effectively avoiding immune recognition system.

A variety of such ligand candidates can be synthesized via solid-phase combinatorial chemistry by using polymer beads, which is a valuable technique that can generate wide variety of similar compounds in a quite economical manner (Fig. 7)[70, 71]. However, the identification of its structure after binding a target protein is a more challenging problem. For easy identification of specific lead

compounds, each compound should be encoded by detectable molecular tags on the polymer support on which the compounds were synthesized[72-75]. However, the stability of chemical tags during the synthesis process is one of the major obstacles, in addition to the complex decoding procedures[76]. On the other hand, optical approaches have been attempted to identify lead compounds directly[77, 78]. Fluorescent dyes or highly fluorescent Quantum dots have been employed for effective encoding. For example, Nie *et al*. inserted Quantum dots into polystyrene microbeads by using swelling methods, as an optical encoding agent[79]. However, this method requires a complicated decoding process that is not suitable for automation. Moreover, the number of coding probabilities is limited owing to the overlap between the emitting fluorescence spectra.

On the other hand, SERS-based encoding method can provide a large number of coding with narrow bandwidths that can prevent signal overlapping (Fig. 8)[80]. Previously reported SERS-based encoding methods permitted the identification of the peptide sequence by encoding each amino acid with the corresponding

SERS NPs[81]. However, the kinds of chemicals that can be incorporated into SERS active NPs as a Raman reporter molecule are limited, although the SERS signals can tag much more signals than other methods such as fluorescence. Therefore, a new kind of SERS tagging method is needed to cover the whole sequence of peptides/peptoids during combinatorial synthesis of peptide or peptoid ligands.

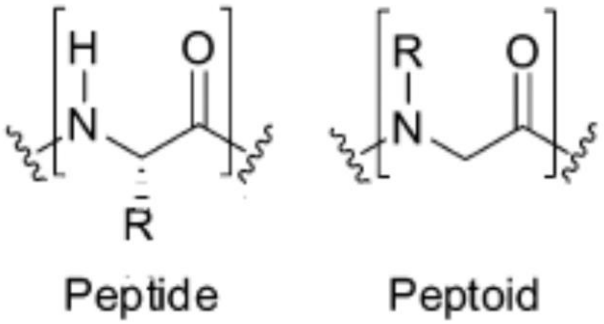

Figure 6. Comparison of structures of peptide and peptoid[82].

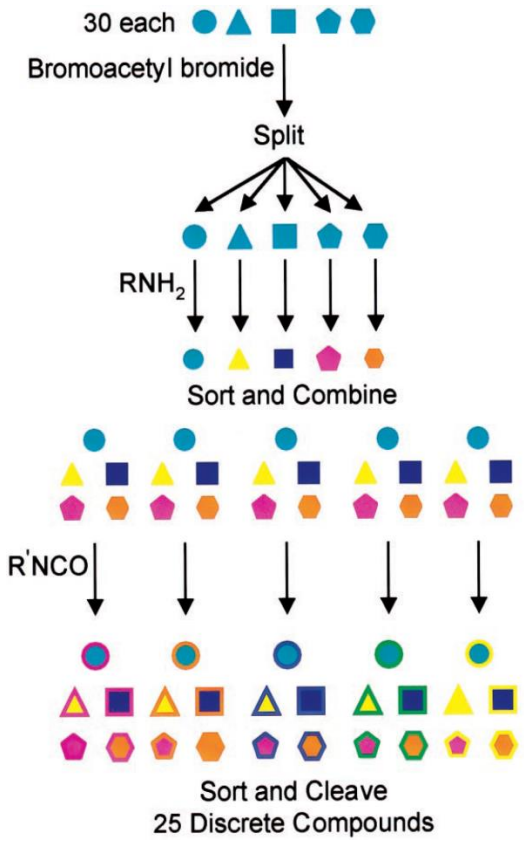

Figure 7. Schematic illustration of combinatorial chemistry[71].

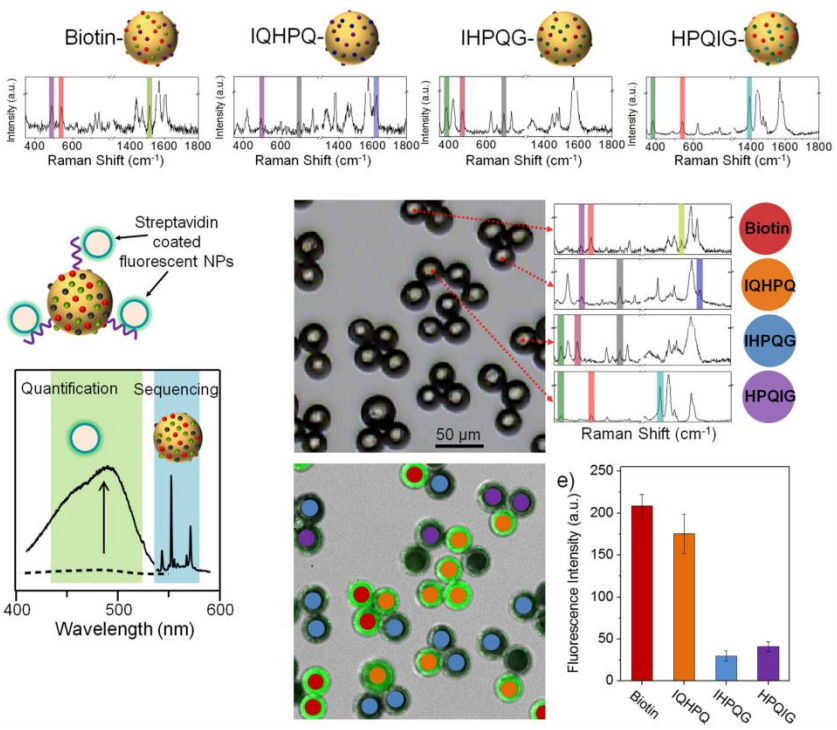

Figure 8. Results of on-bead screening of peptide ligand by SERS[81].

4. Research Objectives

In chapter 1, tri-functional NPs (MF-SERS dots) composed of clustered Fe_3O_4 NPs at core part, assembled Ag NPs, and a silica shell layer containing fluorescent dye, are described. Superparamagnetic Fe_3O_4 NPs clusters are incorporated into the nanostructure for strong response to a magnet field. Strong SERS signal can be generated by MF-SERS dots, arising from the gaps between the assembled Ag NPs. After the internalization into MDA-MB-231 cells, the SERS signal from MF-SERS dots are collected and MF-SERS dots are easily visualized by confocal microscope with their fluorescence. Moreover, MF-SERS dots-containing cells can be separated by a magnet and the separated cells are analyzed by fluorescence activated cell sorting (FACS) system.

In chapter 2, an encoding method that can be used to idenfity peptoid sequences by a SERS silica micro-disks is described. The designed silica micro-disks can be distinguished by the number of holes inside the micro-disks. The SERS property is introduced on

the silica micro-disks by the formation of silver NPs and treatment of Raman reporter molecules. The silica-coated Ag NPs-assembled silica micro-disks (micro-encoders) is applied during solid-phase synthesis of peptoid, by coding the sequence of peptoid side chain with the number of holes, and type of side chain with SERS signals. Using the micro-encoders, a great number of peptoid libraries can be encoded and identified conveniently.

Chapter I.
Magnetic, Fluorescent, and SERS Active Trifunctional Nanoparticles

1. Experimental Section

1.1. Chemicals and Materials

All reagents were used as received from the suppliers without further purification. Absolute ethanol (Abs. EtOH, 99.9%) was purchased from Carlo Erba (Val de Reuil, France). Oleate-stabilized Fe_3O_4 NPs were purchased from Ocean Nanotech (Springdale, AR, USA). Tetraethyl orthosilicate (TEOS), 3-mercaptopropyltrimethoxysilane (MPTS), bovine serum albumin (BSA), 3-aminopropyltriethoxysilane (APTS), caffeic acid, *N*,*N*‘-diisopropylethylamine (DIEA), polyvinylpyrrolidone (PVP, Mw 10000, 40000), ethylene glycol (EG), silver nitrate ($AgNO_3$, 99.99%), octylamine, 4-bromobenzenethiol (4-BBT), 4-chlorobenzenethiol (4-CBT), 4-fluorobenzenethiol (4-FBT), 3,4-dichlorobenzenethiol (3,4-DCT), rhodamine B isothiocyanate (RITC), *N*-hydroxysuccinimide (NHS), 4-(dimethylamino)pyridine (DMAP), and *N*,*N*´-diisopropylcarbodiimide (DIC) were purchased from Sigma Aldrich (St. Louis, MO, USA). (2-(1*H*-Benzotriazole-1-yl)-1,1,3,3-tetramethyluronium hexafluorophosphate (HBTU)

and hydroxybenzotriazole (HOBt) were purchased from Bead Tech (Ansan, Korea). Isopropyl alcohol (IPA), ethyl alcohol (EtOH, 95%), *N*,*N*'-dimethylformamide (DMF), *N*-methyl-2-pyrrolidone (NMP), methylene chloride (MC), diethyl ether, and aqueous ammonium hydroxide (NH_4OH, 27 wt.% in water) were purchased from Daejung (Siheung, Korea). Dulbecco's modified Eagle's medium (DMEM) with high glucose and fetal bovine serum (FBS) were purchased from HyClone Laboratories (Logan, UT, USA). The CD44 antibody was purchased from Abcam (Cambridge, MA, USA). TOPRO-3 was purchased from Invitrogen (Carlsbad, CA, USA).

1.2. Intruments

Transmission electron microscope (TEM) images of NPs were obtained using a Carl Zeiss LIBRA 120 (Oberkochen, Germany), and a JEOL JEM-3000F (Tokyo, Japan) was used for energy-dispersive X-ray spectroscopy (EDX) mapping imaging analysis. SERS measurements were performed using a micro-Raman system (LabRam 300, JY-Horiba). Extinction properties of NP samples were analyzed using a UV/Vis spectrophotometer (Mecasys OPTIZEN POP, Daejeon, Korea). Photoluminescence intensities were obtained using a fluorescence spectrophotometer (Model Cary Eclipse, Agilent Technologies, Santa Clara, CA, USA). Field-dependent magnetization of dried MF-SERS dots was measured using a PPMS-14 (Quantum Design, USA). Fluorescence microscopic images were obtained using a confocal laser scanning microscope (Olympus FV-1000 spectral, Tokyo, Japan). FACS analysis was conducted using a FACSCalibur Flow Cytometer (BD Biosciences, Franklin Lakes, NJ, USA).

1.3. Preparation of MF-SERS Dots

Oleate-stabilized Fe_3O_4 NPs (2.5 mg in 100 μL of chloroform) and 60 mg of PVP (Mw = 10000) were placed in DMF/MC co-solvent (5 mL, 1:1 v/v) and heated for 18 h at 100 °C. Then, the reaction mixture was cooled to 25 °C and poured slowly into 10 mL of diethyl ether. The mixture was centrifuged (4500 rpm, 5 min), and then re-dispersed in EtOH. The silica NPs were synthesized by the Stöber method. TEOS (1.6 mL) and NH_4OH (4 mL) were added to Abs. EtOH (40 mL) and stirred for 20 h at 25 °C. The reaction mixture was washed several times with EtOH by centrifuging at 7000 rpm for 15 min. To introduce amine groups onto the surface of the silica NPs, silica NPs (40 mg in 20 mL EtOH) were incubated with APTS (100 μL) and NH_4OH (100 μL) for 18 h at 25 °C. The reaction mixture was washed several times with EtOH, and then, re-dispersed in NMP. The resulting amine-functionalized silica NPs (20 mg in 5 mL DMF) were mixed with caffeic acid (7.2 mg) and one equivalents of HBTU, HOBt, and DIEA, and then reacted for 3 h at 25 °C. The reaction mixture was washed several times with

DMF. The catechol-functionalized silica NPs (1 mg in 5 mL DMF) and the PVP-stabilized Fe_3O_4 NPs (0.4 mg in 5 mL EtOH) were mixed and sonicated for 1 h at 25 °C, and then, the reaction mixture was washed several times with EtOH. For the silica coating, TEOS (50 μL) and NH_4OH (100 μL) were added to the Fe_3O_4 NP-embedded silica NPs (1 mg in 5 mL EtOH) and reacted for 18 h at 25 °C (M-Silica NPs). The reaction mixture was washed several times with EtOH. For introduction of thiol groups onto the surface of the M-Silica NPs, the M-Silica NPs (1 mg in 1 mL EtOH) were mixed with MPTS (50 μL) and NH_4OH (10 μL) and reacted for 1 h at 50 °C. The reaction mixture was washed several times with EtOH. For introduction of Ag NPs, thiolated M-Silica NPs (1 mg in 25 μL EtOH) were poured into $AgNO_3$ solution (1.25 mg in 1 ml of EG), and then 2 μL of octylamine was injected into the solution. The resulting reaction mixture (Ag-M-Silica NPs) was reacted for 1 h at 25 °C, and then washed several times with EtOH. Four compounds (3,4-DCT, 4-CBT, 4-BBT, and 4-FBT) were selected as Raman reporter molecules. Ag-M-Silica NPs (0.5 mg) were mixed with each Raman reporter molecule solution (10 mM, 1 mL in EtOH) and

reacted for 1 h at 25 °C. The reaction mixture was washed several times with IPA. For silica coating, PVP (1 mg, Mw = 40000), water (60 μL), TEOS (10 μL), and NH_4OH (10 μL) were added to the Raman reporter molecule-treated Ag-M-Silica NPs and reacted for 18 h at 25 °C. The silica-coated Ag-M-Silica NPs were washed several times with IPA. For introduction of fluorescent silica shells, RITC (8 mM in 50 μL EtOH) was reacted with APTS (19.2 mM in 500 μL EtOH) for 16 h at 25 °C. A portion of the resulting solution (20 μL) was added to the silica-coated Ag-M-Silica NPs (in 2 mL IPA), along with water (400 μL), TEOS (2 μL), and NH_4OH (10 μL). The mixture was incubated for 18 h at 25 °C, and the resulting fluorescence shell-coated Ag-M-Silica NPs (MF-SERS dots) were washed several times with EtOH. For introduction of amine groups, the MF-SERS dots (0.5 mg in 1 mL EtOH) were incubated with APTS (50 μL) and NH_4OH (10 μL) and reacted for 1 h at 25 °C. The reaction mixture was washed several times with EtOH, and the resulting amine-functionalized MF-SERS dots (MF-SERS $dots_{amine}$) were re-dispersed in phosphate buffered saline (PBS, 10 mM, pH 7.4). For introduction of antibodies onto the MF-SERS dots, MF-

SERS $dots_{amine}$ were re-dispersed in NMP (0.5 mL) and reacted with succinic anhydride (1.75 mg) and DIEA (3.05 μL) for 2 h at 25 °C. The reaction mixture was washed several times with DMF. The resulting carboxyl group-ended MF-SERS dots in 200 μL DMF were reacted with NHS (40 mg), DMAP (4.2 mg), and DIC (54 μL) for 2 h at 25 °C. The reaction mixture was washed several times with PBS solution at 4 °C. CD44 antibody (25 μg) was added to the NHS activated MF-SERS dots (in 200 μL PBS solution) and reacted for 1 h at 25 °C. The reaction mixture was washed with PBS solution containing 0.1 wt.% TWEEN 20, and the antibody-conjugated MF-SERS dots (MF-SERS $dots_{Ab}$) were then re-dispersed in PBS solution.

1.4. Cell Culture and Internalization of MF-SERS Dots

MDA-MB-231 cells (breast cancer epithelial cell line, purchased from American Type Culture Collection, ATCC HTB-26) and HepG2 cells (liver epithelial cell line, purchased from ATCC, ATCC HB-8065) were cultured in Dulbecco's modified Eagle's medium with high glucose (HyClone Laboratories, Logan, UT, USA) supplemented with 10% fetal bovine serum (HyClone Laboratories) and 100 U/mL of penicillin (Welgene, Daegu, Korea) at 37 °C in humidified air containing 5% CO_2. To determine the cellular binding of MF-SERS $dots_{amine}$ to the cells, MDA-MB-231 cells were seeded onto a 24-well plate with cover glass (Paul Marienfeld GmbH, Lauda-Königshofen, Germany) at a density of 2.0×10^5 cells and incubated at 37 °C. After 16 h of incubation, the cover glass was blocked with 3% BSA in PBS at room temperature for 30 min. After washing with PBS twice, 500 μL of media containing 0.25 mg/mL of MF-SERS $dots_{amine}$ was added to the cells and incubated again at 37 °C for 2 h. The cells were washed twice with PBS and fixed with 4% paraformaldehyde (w/v) at

room temperature for 1 h. The cells were washed again with PBS, and the nuclei were stained using TOPRO-3 (1 μM in PBS) at room temperature for 30 min. The cells were then mounted on microscope slides (Paul Marienfeld GmbH) with ProLong Gold antifade reagent (Invitrogen) and observed using a confocal laser scanning microscope. The orange fluorescence from the MF-SERS $dots_{amine}$ and the pseudo-blue fluorescence from TOPRO-3 stained nuclei were monitored and merged with the bright field cell images. In addition, SERS signals from the MF-SERS $dots_{amine}$-treated cells mounted on microscope slides were obtained by point-by-point mapping using a 660 nm laser line at a power of 11.8 mW with a 1-μm step size for 1 s.

1.5. Magnetic Isolation and Flow Cytometry Analysis

Fresh medium (2.5 mL) was prepared in a 5 mL tube (Eppendorf, Hauppauge, NY, USA) containing MDA-MB-231 cells (2.0×10^5) with or without MF-SERS $dots_{amine}$ (20 μL, 0.25 mg/mL). After incubation at 37 °C for 2 h, a strong magnet (4000 gauss) was placed on one side of the tube, followed by a further 2 h incubation at room temperature. The cells submerged at the bottom of the tube were carefully removed, and only the cells attracted to the wall by the magnet were collected and quantified by FACS analysis.

1.6. Antibody-specific Binding of MF-SERS Dots on MDA-MB-231 Cells

The specific binding of the MF-SERS $dots_{Ab}$ to antigen-expressing cells was monitored by observing orange fluorescence of the MF-SERS $dots_{Ab}$ on the cells using a confocal microscope. The CD44-positive (+) cell line (MDA-MB-231 cells) and the CD44-negative (-) cell line (HepG2 cells) were grown in the wells of a 12 well plate with cover glass at a density of 1.0×10^6 cells. The cells were fixed with 4% paraformaldehyde at room temperature for 1 h and blocked with 3% BSA. After washing three times with PBS, 1 mL of PBS containing MF-SERS $dots_{Ab}$ (0.25 mg/mL) or MF-SERS dots (0.25 mg/mL) were added to the cells and incubated at 4 °C for 2 h. The primary CD44 antibody (110 μg/mL) and fluorescence-conjugated secondary antibodies (110 μg/mL, Alexa Fluor 488) were also treated to MDA-MB-231 cells or HepG2 cells at 4 °C for 2 h as a control. The cells were washed three times with PBS and visualized using a confocal microscope after nuclei staining as mentioned above.

2. Results and Discussion

2.1. Synthesis of MF-SERS Dots

The MF-SERS dots were synthesized by introducing multiple functional layers, including clustered Fe_3O_4 NPs, assembled Ag NPs, and a fluorescent dye-conjugated silica shell layer to provide SERS-magnetic-fluorescence tri-functionality, followed by conjugation of an antibody for biotargeting (Fig. 9). The layers of Fe_3O_4 NP clusters provided a strong response to an external magnetic field due to their superparamagnetism, and assembled Ag NPs afforded a strong SERS signal triggered by the formation of hot spots. Fig. 10 shows the synthetic procedure for preparing the MF-SERS dots. Silica NPs were used as a backbone structure to immobilize the NPs, as they can be synthesized and modified easily. The silica NPs were synthesized by the Stöber method[83] with a narrow size distribution (250±10 nm), as shown in Fig. 11a. Amine groups were then introduced onto the silica NPs using APTS. To immobilize the superparamagnetic Fe_3O_4 NPs on the surface of the

silica NPs, amine-functionalized silica NPs were coupled with caffeic acid to introduce catechol groups, which are known to have a strong affinity for Fe_3O_4 NPs[84]. To avoid aggregation of the Fe_3O_4 NPs in the amphiphilic solvent when reacting with catechol-functionalized silica NPs, oleate-stabilized Fe_3O_4 NPs underwent a ligand exchange process. Oleate-stabilized Fe_3O_4 NPs were treated with PVP at 100 °C, and then cooled to room temperature. The resulting Fe_3O_4 NPs showed good dispersion in amphiphilic solvents, which confirms that the oleate ligands were replaced by PVP. The PVP-stabilized Fe_3O_4 NPs were then mixed with the catechol-functionalized silica NPs to immobilize the Fe_3O_4 NPs on the silica NPs. A silica layer with a thickness of 10 nm was then introduced onto the Fe_3O_4 NP-embedded silica NPs to allow further surface modification. The resulting silica-coated Fe_3O_4 NP-embedded silica NPs (M-Silica NPs) contained 400 units of Fe_3O_4 NPs, as confirmed by TEM (Fig. 11b).

Next, the surface of the M-Silica NPs was functionalized with thiol groups using MPTS to attract the Ag ions and aid the formation of Ag NPs[85]. Ag^+ ions were reduced by using octylamine,

and large amounts of Ag NPs were assembled on the surface of the M-Silica NPs (Fig. 11c). Thiol group containing aromatic compounds were used as Raman reporter molecules. The surface of the Ag NPs-assembled M-Silica NPs (Ag-M-Silica NPs) was treated with the Raman reporter molecules, and then coated with another silica layer to provide chemical stability and biocompatibility. To introduce the fluorescent shell, RITC was conjugated with APTS[39]. The silicate monomer-conjugated RITC was then reacted with the silica-coated Ag-M-Silica NPs. The thickness of the outer silica layer of the NPs was ca. 50 nm, as measured from a TEM image (Fig. 11d, inset). The synthesized fluorescent shell-coated Ag-M-Silica NPs (MF-SERS dots) had uniform size distributions of 400±40 nm (Fig. 11d). The chemical compositions of the MF-SERS dots were investigated by EDX. The locations of the Si, Ag, and Fe atoms in the MF-SERS dots are clearly shown in Fig. 12a–d. These results prove that the MF-SERS dots were successfully fabricated.

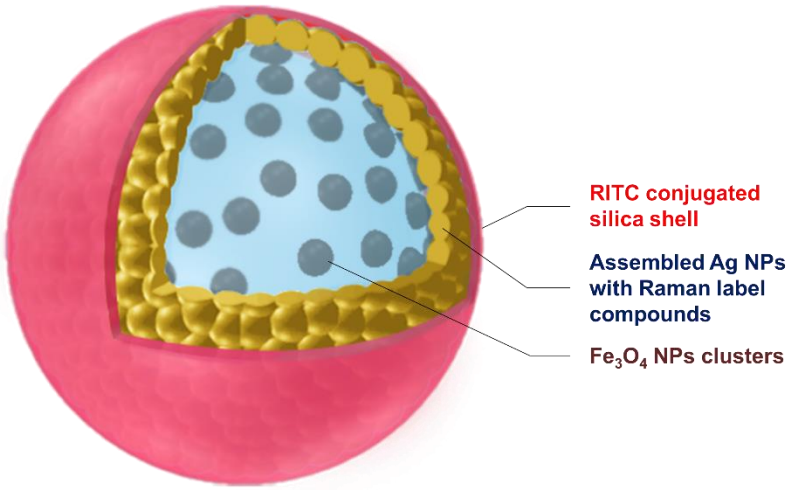

Figure 9. The structure of MF-SERS dots with magnetic-fluorescence-SERS trifunctionality and conjugated antibody.

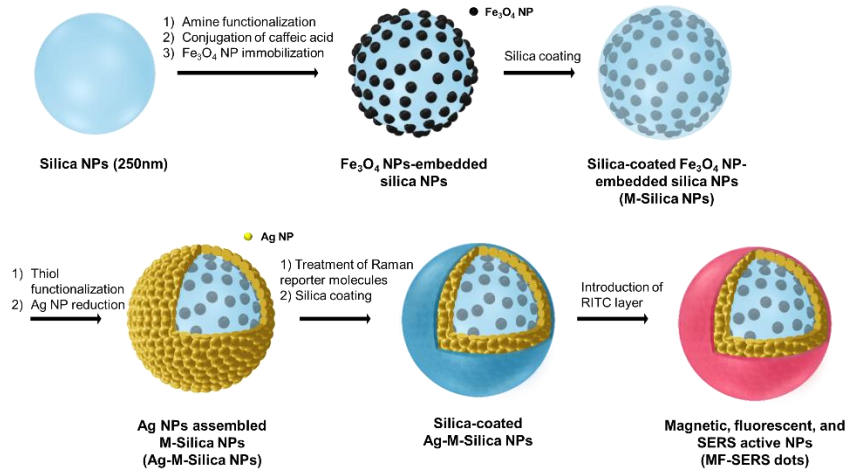

Figure 10. Overall scheme for the synthesis of MF-SERS dots.

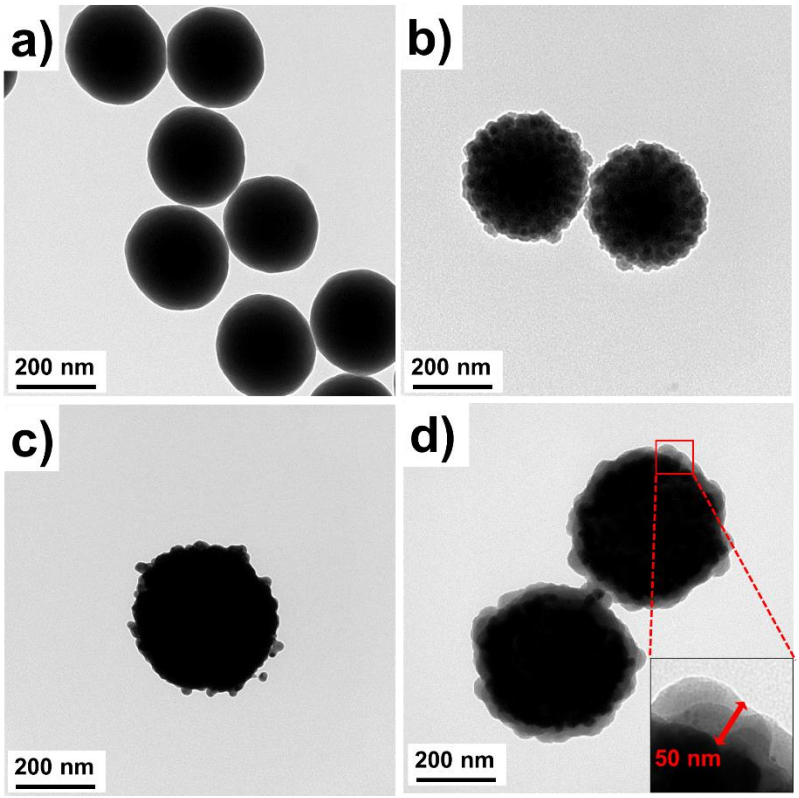

Figure 11. Transmission electron microscopic (TEM) images of a) silica NPs, b) M-Silica NPs, c) Ag-M-Silica NPs, and d) MF-SERS dots. The inset shows silica layer of MF-SERS dots.

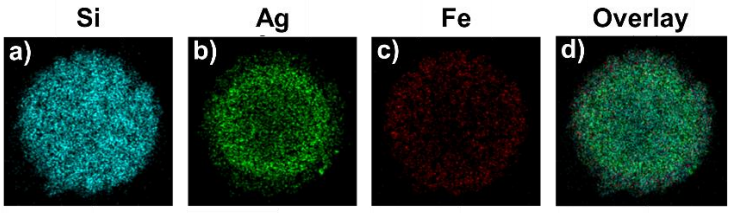

Figure 12. EDX mapping images showing each elements of MF-SERS dots including a) Si atoms, b) Ag atoms, c) Fe atoms, and d) overlay image of all elements.

2.2. Characterization of MF-SERS Dots

In order to provide MF-SERS dots with multiplexing capability, four Raman reporter molecules (4-FBT, 4-CBT, 4-BBT, and 3,4-DCT) were used. SERS signals were obtained from the Raman reporter molecule-treated MF-SERS dots, and unique SERS patterns of the respective molecules could be clearly distinguished by their narrow bands at 386 cm^{-1} (4-FBT), 488 cm^{-1} (4-BBT), 541 cm^{-1} (4-CBT), and 565 cm^{-1} (3,4-DCT) (Fig. 13a). Among the Raman reporter molecules, even asymmetric aromatic compound (3,4-DCT), which usually gives low SERS signals, could also generate strong SERS signals due to the bumpy structure of Ag NPs layer of the MF-SERS dots. Thus, various aromatic compounds can be used as Raman reporter molecules, expanding the multiplexing capability of MF-SERS dots.

The extinction spectra of NPs during every synthetic step for MF-SERS dots fabrication are shown in Fig. 14. Being different from the absorption band of the M-Silica NPs, the Ag-M-Silica NPs showed an absorption band at ca. 400 nm and a broad band

ranging from visible to NIR region. This was mainly due to the plasmonic property of the Ag NPs and their aggregate. The valley feature at ca. 500 nm in this spectrum disappeared in the absorption spectrum of the MF-SERS dots due to the emission band of RITC within the outer shell of MF-SERS dots while the overall feature of the plasmonic extinction maintained in the MF-SERS dots. This result shows that the aggregated state of Ag NPs were well preserved after the silica shell coating step as confirmed by TEM (Fig. 11d), and thus plasmonic properties of the Ag NPs were preserved during the NP's synthesis.

We also analyzed the photoluminescence spectrum of the MF-SERS dots with a 540 nm photo-excitation (Fig. 15). An emission band at 580 nm was observed from MF-SERS dots, corresponding to the emission band of RITC, indicating that fluorescent RITC molecule was well introduced in the silica shell layer.

To confirm the magnetic properties of the MF-SERS dots, the field-dependent magnetization was measured at 300 K (Fig. 16). The magnetization curve exhibited a saturated magnetization of 2.1 emu/g without coercivity, indicating that the MF-SERS dots

were superparamagnetic. In addition, MF-SERS dots were attracted to a magnet (4000 gauss) within 10 min, which is more advantageous for cell separation than single magnetic NPs (Fig. 16, inset).

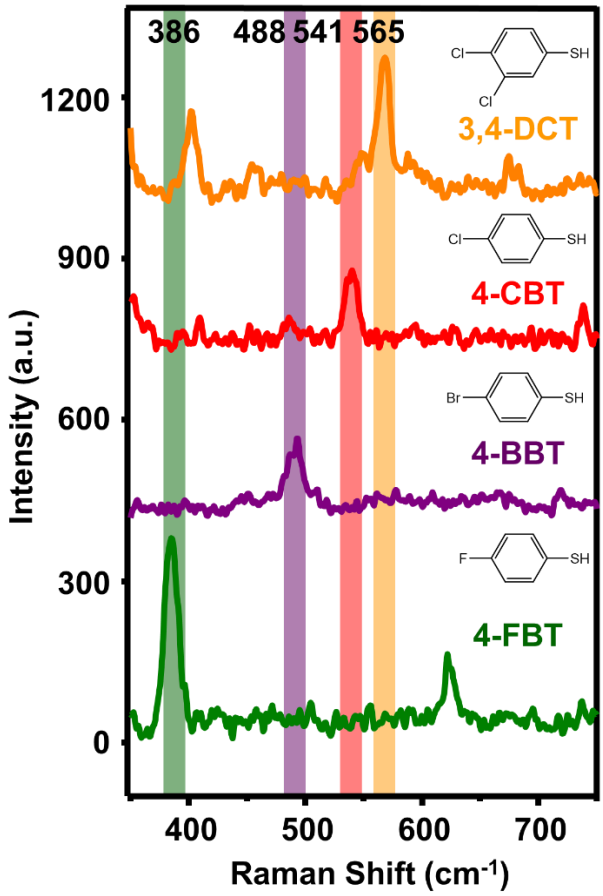

Figure 13. SERS signals from MF-SERS dots. The type of Raman reporter molecules are 3,4-DCT, 4-CBT, 4-BBT and 4-FBT.

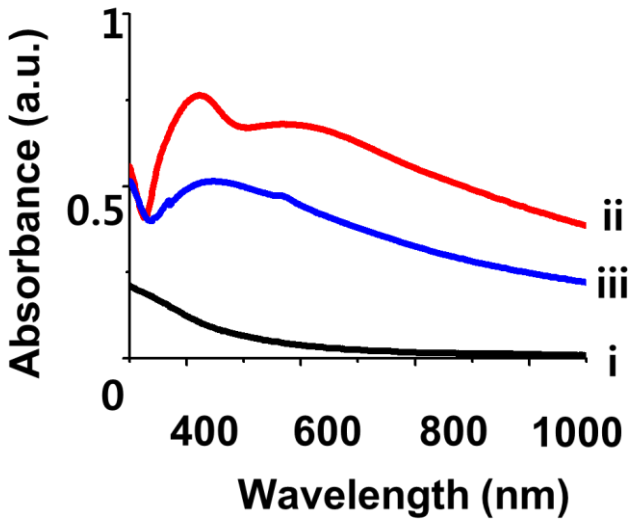

Figure 14. Absorption spectra of NPs in each steps (i: M-Silica NPs, ii: Ag-M-Silica NPs and iii: MF-SERS dots).

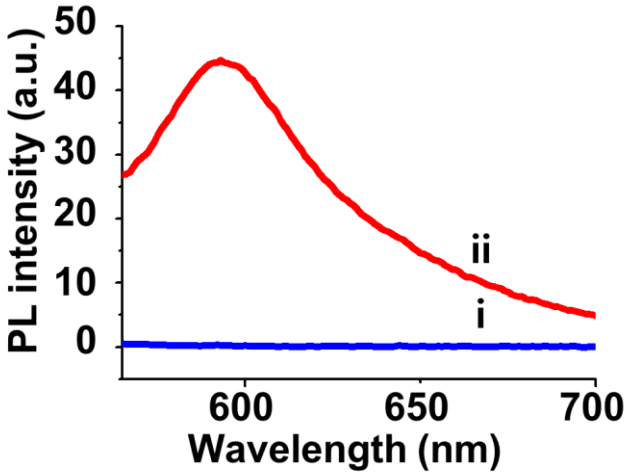

Figure 15. Photoluminescence spectra of i) silica coated Ag-M-Silica NPs and ii) MF-SERS dots.

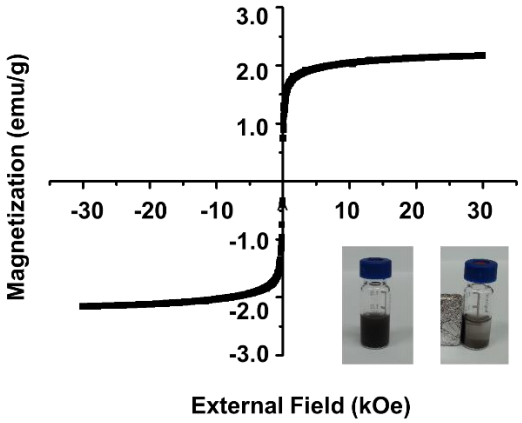

Figure 16. Hysteresis loop of the MF-SERS dots. The inset shows photographic images of the MF-SERS dots before (left) and after (right) magnet attraction.

2.3. Internalization of MF-SERS Dots into MDA-MB-231 Cells

Various studies have been reported on the interaction of NPs (~400 nm) with cells. NPs of approximately 400 nm size are known to bind to cells with *ca.* 50% being absorbed into the cell[86]. In addition, NPs with positive surface charges can have strong interactions with cells because the surface of the cells is negatively charged[87]. Thus, the surface of the MF-SERS dots was modified with APTS. The amine-functionalized MF-SERS dots (MF-SERS $dots_{amine}$) were then incubated with MDA-MB-231 cells on a glass slide at 37 °C for 2 h. The cells with MF-SERS $dots_{amine}$ were visualized by confocal microscopy to evaluate whether cellular uptake had occurred (Fig. 17). After proper washing, significant amount of orange fluorescence was observed from the MF-SERS $dots_{amine}$ around the nuclei of the MDA-MB-231 cells (blue). These results suggest that the MF-SERS $dots_{amine}$ (~400 nm) could be internalized into the cell.

SERS signals from MF-SERS dots-containing cells were detected using point-by-point mapping using 660 nm laser

excitation at a power of 11.8 mW with a step size of 1 μm and an exposure time of 1 s per point. The SERS map was then overlaid with the corresponding bright-field optical image, as shown in Fig. 18. The SERS spectrum of the 4-FBT, that had been labeled as a Raman reporter molecules, could be obtained from regions i), ii), and iii) in Fig. 4b. The signal intensity in the SERS map was based on the height of the most intense peak of the 4-FBT spectrum at 1075 cm^{-1}. As a result, SERS signals from MF-SERS dots could be collected even from cells.

Next, we attempted to separate the MF-SERS dots-containing cells using an external magnetic field. The MF-SERS $dots_{amine}$ were mixed with MDA-MB-231 cells that were floating freely in the cell culture medium at 37 °C for 2 h. Then, a magnet was placed at the side of the cell mixture until the cells were pulled toward the magnet. The pulled down cells were collected and analyzed by FACS. As a result, cells with enhanced fluorescence emission were separated by FACS, as shown in Fig. 19 (population ii). Because the cells contain many MF-SERS dots, they exhibited stronger fluorescence intensity than untreated MDA-MB-231 cells

(population i in Fig. 19), resulting in a shift to higher fluorescence intensity in the FACS analysis. Furthermore, pure MF-SERS dots were analyzed by FACS, and the results were compared to those obtained with the MDA-MB-231 cells (Fig. 20). No particles were detected by FACS, showing that MF-SERS dots without interaction with cells during incubation period cannot be detected by FACS. Thus, these results indicate that MF-SERS dots-containing cells were readily separated by external magnetic field.

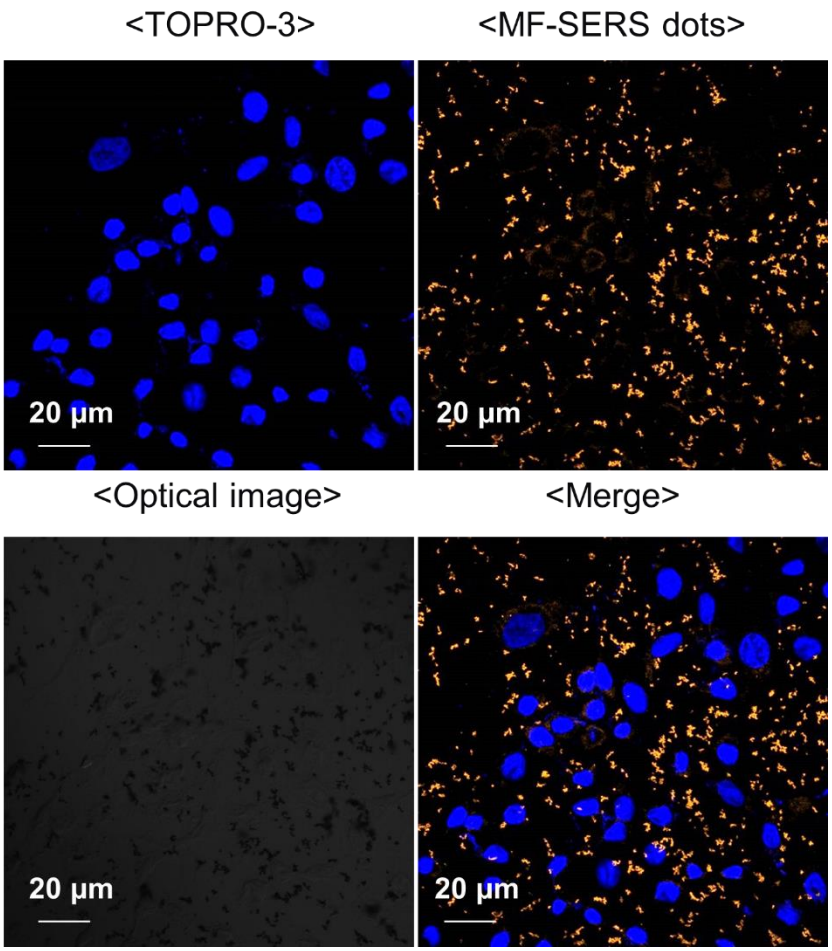

Figure 17. Fluorescence microscopy images of MDA-MB-231 cells incubated with MF-SERS dots and stained by TOPRO-3 (pseudo-blue fluorescence), showing the internalization of MF-SERS dots (orange fluorescence) into MDA-MB-231 cells.

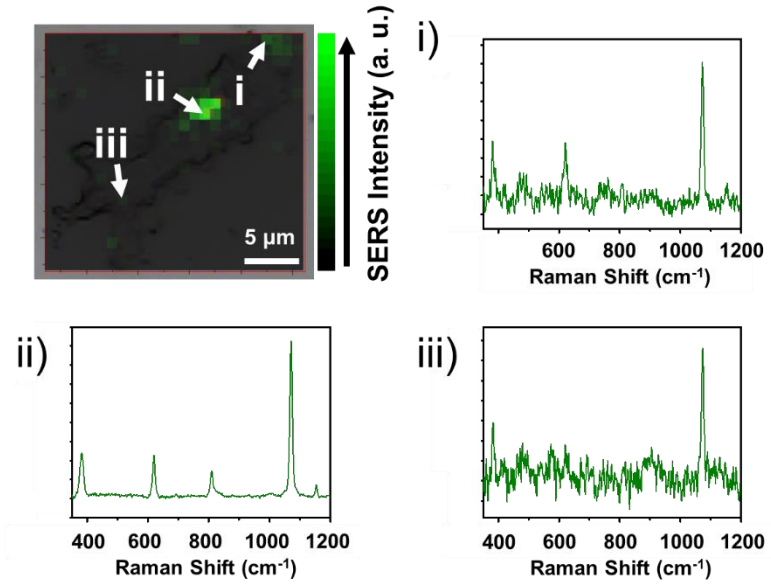

Figure 18. The SERS intensity map of MF-SERS dots in MDA-MB-231 cells, overlaid with the corresponding bright-field optical image. 4-FBT was used as Raman reporter molecules and Raman spectrum of 4-FBT could be obtained from each positions (i, ii, and iii).

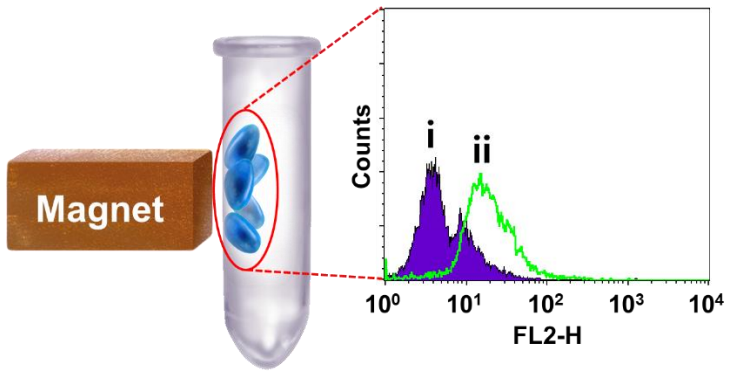

Figure 19. Flow cytometry analysis of MDA-MB-231 cells as control (population i) and cells collected from the wall after treated with MF-SERS dots and pulled by magnet (population ii).

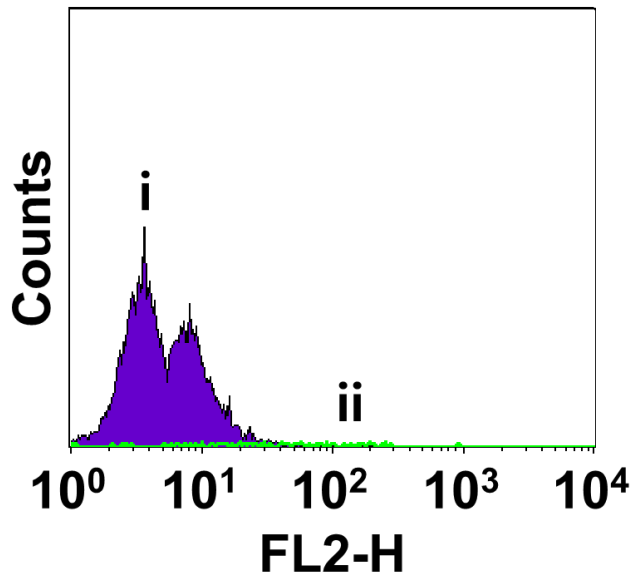

Figure 20. Flow cytometry analysis of (i) MDA-MB-231 cells and (ii) only MF-SERS dots.

2.4. Specific Binding of CD44 Antibody-conjugated MF-SERS Dots to MDA-MB-231 Cells

The antigen-specific binding of the CD44 antibody-conjugated MF-SERS dots (MF-SERS dots$_{Ab}$) to CD44-expressing cells was investigated. First, the surface of the MF-SERS dots was modified via EDC/NHS coupling reaction in order to immobilize antibodies on the MF-SERS dots[88]. Briefly, the surface of the MF-SERS dots was functionalized with amine groups using APTS. Then, the amine groups on the surface of the MF-SERS dots were reacted with succinic anhydride to transform to carboxyl groups. The carboxyl groups were then activated by EDC/NHS for CD44 antibody coupling. After the CD44 antibody was conjugated to carboxyl groups, and the resulting MF-SERS dots$_{Ab}$ were incubated with CD44-expressing MDA-MB-231 cells at 4 °C for 2 h. A schematic illustration of the antigen-specific binding of the MF-SERS dots with the CD44-expressing cells is shown in Fig. 21. We examined the CD44 expression in MDA-MB-231 or HepG2 cells by immunostaining by green fluorescence (Fig. 22). The

green fluorescence for the CD44 antigen was not observed in the HepG2 cells, while strong green fluorescence was clearly observed in the MDA-MB-231 cells. In the MDA-MB-231 cells, the orange fluorescence of the MF-SERS $dots_{Ab}$ was also clearly observed at the periphery of the cells with pseudo-blue fluorescent nuclei (Fig. 23). However, the orange fluorescence was rarely observed due to the absence of CD44 antibody conjugation or the CD44-negative HepG2 cells (Fig. 24). These results prove that the MF-SERS $dots_{Ab}$ selectively recognized the CD44 antigen in the CD44-expressing MDA-MB-231 cells.

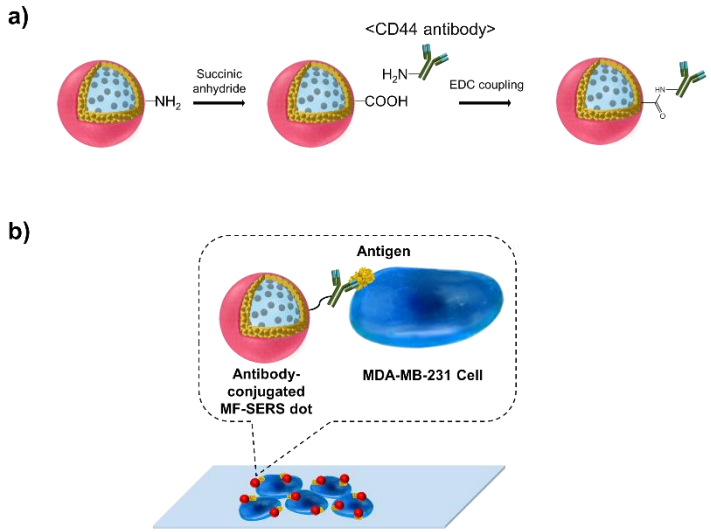

Figure 21. a) Conjugation of CD44 antibody on MF-SERS dots. b) Schematic illustration of the recognition of antibody-conjugated MF-SERS dots on antigen containing cells.

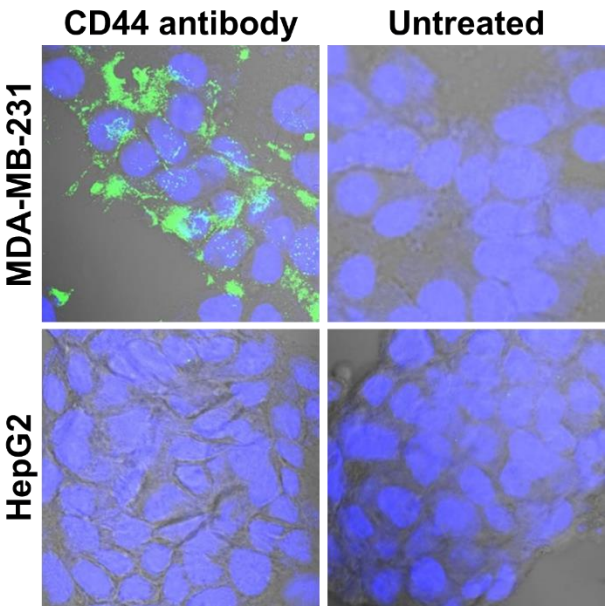

Figure 22. Confocal fluorescence microscopy images of MDA-MB-231 cells treated with CD44 antibodies or untreated MDA-MB-231 cells, and HepG2 cells treated with CD44 antibodies or untreated HepG2 cells at 4 °C for 2 h. The green fluorescence represents the expression of CD44 antigen and pseudo-blue fluorescence shows the nuclei.

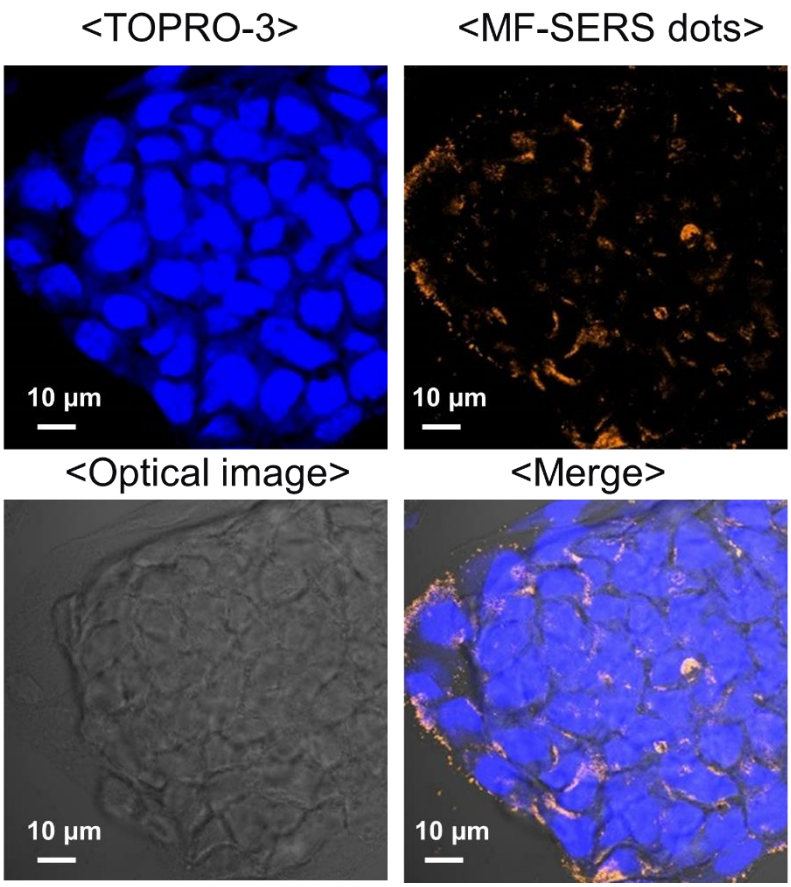

Figure 23. Confocal fluorescence microscopy images of MDA-MB-231 cells treated with CD44 antibody-conjugated MF-SERS dots at 4 °C for 2 h. The fluorescence of MF-SERS dots was monitored by orange fluorescence and the nuclei stained by TOPRO-3 were detected by pseudo-blue fluorescence.

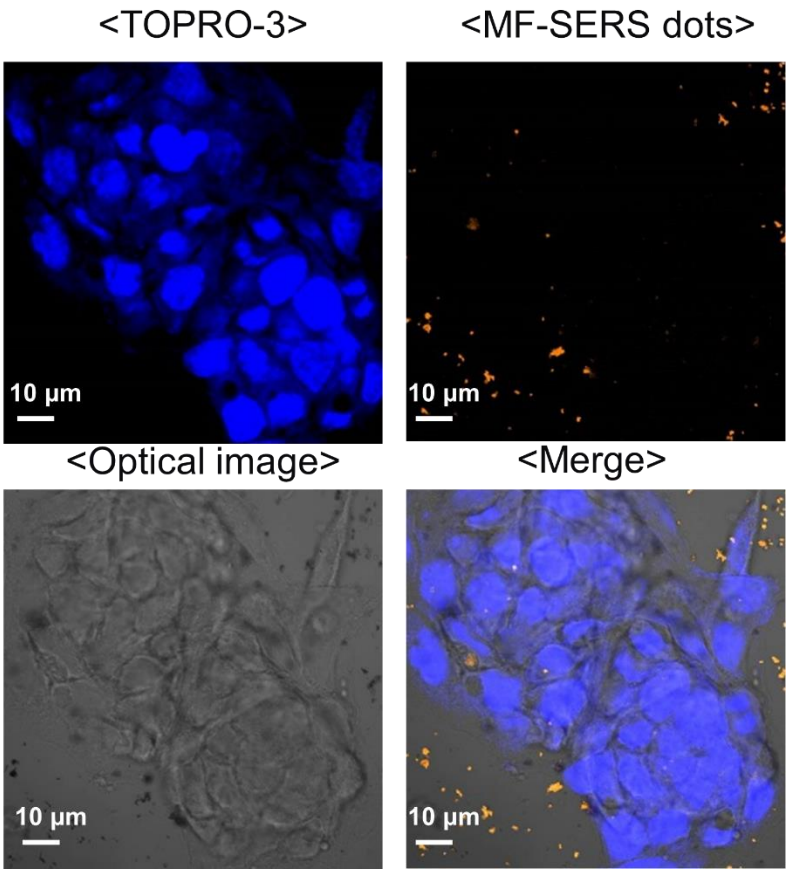

Figure 24. Confocal fluorescence microscopy images of HepG2 cells treated with CD44 antibody-conjugated MF-SERS dots at 4 °C for 2 h.

3. Conclusion

MF-SERS dots containing magnetic, fluorescence, and SERS properties were fabricated by immobilizing superparamagnetic Fe_3O_4 NP clusters on silica NPs, followed by assembling Ag NPs on them, and introducing a fluorescent silica layer. SERS signals were successfully obtained from aromatic Raman reporter molecules (4-FBT, 4-CBT, 4-BBT, and 3,4-DCT) coated on the MF-SERS dots, and fluorescence signals were also obtained at the same time. The MF-SERS dots exhibited a strong response to an external magnetic field due to their superparamagnetic property. After the cells were treated with the MF-SERS dots, the cells could be separated from the others using an external magnetic field and identified by FACS analysis. The characteristic features of each modality of the MF-SERS dots, including fluorescence, SERS, and magnetic properties, were preserved after cellular uptake. Moreover, the MF-SERS dots could be modified further with CD44 antibody via an amide coupling reaction, and successfully targeted the CD44-positive cells. The tri-functional NPs with

SERS, magnetic, and fluorescent properties are expected to be useful nanoprobes for cell separation and multiplexed detection.

Chapter II.
On-bead Screening of Ligand Using Graphical and SERS Two-dimensional Micro-encoder

1. Experimental Section

1.1. Chemicals and Materials

All reagents are used without further purification process. Tetraethyl orthosilicate (TEOS), ammonium hydroxide (NH_4OH, 28 wt% in water), 3-mercaptopropyltrimethoxysilane (MPTS), silver nitrate ($AgNO_3$, 99.99%), ethylene glycol, octylamine, *N*,*N*-diisopropylcarbodiimide (DIC), bovine serum albumin (BSA), Streptavidin-conjugated fluorescein isothiocyanate (streptavidin-FITC), bromoacetic acid, acetic anhydride, 2-methoxyethylamine (N_{mea}), *N*-(3-aminopropyl)-2-pyrrolidinone (N_{app}), 1-naphtylmethylamine (N_{nap}), piperonylamine (N_{pip}), isobutylamine (N_{leu}), 4-FBT (4-fluorobenzenethiol), 4-chlorobenzenethiol (4-CBT), and 4-bromobenzenethiol (4-BBT) were purchased from Sigma Aldrich. 2-(1*H*-Benzotriazole-1-yl)-1,1,3,3-tetramethyluronium hexafluoro- phosphate (HBTU), hydroxybenzotriazole (HOBt), (benzotriazol-1-yloxy)tris(dimethylamino)phosphonium hexafluorophosphate

(BOP) were purchased from Bead Tech. Ethanol (EtOH, 95%), isopropyl alcohol (IPA), *N*,*N*-dimethylformamide (DMF), *N*-methyl-2-pyrrolidone (NMP) , methylene chloride (MC), and *N*,*N*-diisopropylethylamine (DIEA) were purchased from Daejung Chemical. Tetrametylammonium hydroxide (TMAH, 20 wt% in water) was purchased from Hyo dong chem ENG. TentaGel (TG) beads were purchased from RappPolymere. Fmoc-photolabile linker (PLL) was purchased from Advanced ChemTech.

1.2. Instruments

Scanning electron microscope (SEM) images of micro-encoders were obtained using a JSM-6701F (JEOL). Energy-dispersive X-ray spectroscopy (EDX) mapping imaging analysis was conducted using a JSM-6701F (JEOL). SERS measurements were performed using a micro-Raman system (LabRam 300, JY-Horiba). Confocal microscope image was obtained using a SP8X (Leica). Electrospray ionization mass spectrometry (ESI-MS) spectrum was obtained using a LTQ (Thermo Finnigan).

1.3. Preparation of Micro-encoders

Silica micro-disks were fabricated by photolithographic process. Silicon oxide layer was formed on 150 mm sized silicon wafer by wet oxidation process at 900 °C. The silicon oxide layer was then covered with photoresist layer that has graphic patterns of shape and holes of silica micro-disks. According to the graphic pattern, designated sections were etched to complete the fabrication of silica micro-disks. After photoresist layer was eliminated, the silica micro-disks were released from silicon wafer by treating with TMAH solution (300 mL) at 80 °C for 1 h. Then, the silica micro-disks containing solution was centrifuged (7000 rpm, 10 min) and washed with water and EtOH several times.

To obtain thiolated silica micro-disks, MPTS (30 μL) and NH_4OH (10 μL) were added to the silica micro-disks (2.1×10^6 units in 1 mL EtOH). The mixture was shaken for 1 h at 25 °C. The resulting thiolated silica micro-disks were centrifuged (7000 rpm, 5 min) and washed several times with EtOH to remove excess reagent. Then, the thiolated silica micro-disks were dispersed in EG (1 mL). For the introduction of Ag NPs, 20 μL of $AgNO_3$ (25

mM in EG) and octylamine (25 mM in EG) solutions were added to the thiolated silica micro-disks dispersion (2.1 x 10^6 units in 1 mL EG). The final concentrations of $AgNO_3$ and octylamine were 0.5 mM. The mixture was stirred for 1 h at 25 °C, centrifuged (3000 rpm, 5 min) and washed several times with EtOH to obatin Ag NPs-assembled silica micro-disks. Three kinds of Raman reporter molecule solutions (4-FBT, 4-CBT, and 4-BBT) were prepared (20 mM, 0.5 mL in EtOH) and mixed with MPTS (40 mM, 0.5 mL in EtOH). Then, the Ag NPs-assembled silica micro-disks (2.1 x 10^6 units) were dispersed in the mixture of Raman reporter molecules (1 mL) and MPTS, and reacted for 1 h at 25 °C. The final concentrations of Raman reporter molecules and MPTS were 10 mM and 20 mM, respectively. The reaction mixture was washed several times with IPA. For silica coating, water (30 μL), TEOS (5 μL), and NH_4OH (5 μL) were added to the Raman reporter molecule-treated Ag NPs-assembled silica micro-disks (2.1 x 10^6 units in 1 mL IPA) and reacted for 18 h at 25 °C. The silica-coated Ag NPs-assembled silica micro-disks (micro-encoders) were washed several times with EtOH. To obtain the

SERS spectra from the micro-encoders, point-by-point SERS mapping was conducted with a 1 μm step size for 1s using a 532 nm laser at a power of 0.06 mW.

1.4. Tagging TG Beads by Embedding Micro-encoders

For embedding micro-encoders on TG beads, 1 mg of TG beads (2.86×10^3 beads) in 1 mL DMF were treated with 1 mL of micro-encoder solution (2.86×10^4, 1.43×10^5, 2.86×10^5, 5.72×10^5, 1.14×10^6, and 2.28×10^6 units in 1 mL EtOH). The mixture was reacted for 1 h at 25 °C, and washed several times with DMF.

For the conjugation of photolabile linker (PLL) to TG beads, 10 mg of TG beads were reacted with 1.5 equivalent of PLL, 3 equivalent of BOP and 3 equivalent of DIEA for 2 h at 25 °C. Then, the reaction mixture were washed with DMF and MC, several times each. For capping the residual amine groups on TG beads, the beads were reacted with 5 equivalent of acetic anhydride and 5 equivalent of DIEA for 30 min at 25 °C, and washed with DMF and MC, several times each. Fmoc groups were deprotected by reacting the TG beads (10 mg) with piperidine (3 mL, 20 wt% in DMF) for 1 h at 25 °C.

For embedding micro-encoders on the beads, bare TG beads or PLL-coupled TG beads (10 mg, 1 mL in DMF) were mixed with

micro-encoders (1.4 x 10^6 units in 1 mL EtOH), and incubated for 1 h at 25 °C. The reaction mixtures were washed with DMF several times. The stability of micro-encoders on PLL-coupled TG beads was examined by reacting the beads (10 mg) with 20 equivalent of DIC in 2 mL DMF or incubating the beads (10 mg) with 2 mL MC for 30 min at 25 °C. The SERS spectra were obtained from the micro-encoders on the beads, using point-by-point SERS mapping with a 1 μm step size for 1s using a 532 nm laser at a power of 0.06 mW.

1.5. Optimization of Peptoid Coupling Reaction on TG Beads

The micro-encoders (2.8×10^6 units in 1 mL EtOH) were added to TG beads (10 mg, 1 mL in DMF) for 1 h at 25 °C. The reaction mixtures were washed with DMF several times. Then, the peptoid synthesis condition was optimized by adjusting the added amounts of bromoacetic acid and primary amines. The beads (10 mg, 2 mL in DMF) were reacted with 5, 10, and 20 equivalent of bromoacetic acid and 20 equivalent of DIC for 30 min at 25 °C. The reaction mixtures were washed with DMF and MC, several times each. From the results of SEM images and acetaldehyde/chrolanil test, 10 equivalent of bromoacetic acid was determined to be the optimal condition. Therfore, the beads which had been treated with 10 equvalent of bromoacetic acid were used for further peptoid coupling reaction. The beads (10 mg, 2 mL in NMP) were then reacted with 10, 20, and 50 equivalent of primary amine for 30 min at 25 °C, and washed several times with NMP and MC.

1.6. Encoding Peptoid Sequence on TG Beads Using Micro-encoders

Before the synthesis and encoding of pentapeptoid which is composed of N_{mea}, N_{app}, N_{nap}, N_{pip}, and N_{leu}, PLL-coupled TG beads were prepared as described in Section 1.4. The PLL-coupled TG beads (10 mg, 2 mL in DMF) were reacted with 10 equivalent of bromoacetic acid and 20 equivalent of DIC for 30 min at 25 °C, and washed with DMF and MC several times. Then, the beads (10 mg, 2 mL in NMP) were reacted with 10 equivalent of primary amine for 30 min at 25 °C, and washed with NMP and MC several times. After the conjugation of N_{nap}, 1 mL of micro-encoders which contain 1 hole and 4-FBT (micro-encoders$_{(1)(4\text{-FBT})}$, 2.8×10^7 units in 1 mL EtOH) were added to the beads (10 mg, 1 mL in DMF). The mixture was reacted for 1 h at 25 °C, and washed with EtOH and DMF several times. After the conjugation of N_{pip}, 1 mL of micro-encoders which contain 2 hole and 4-CBT (micro-encoders$_{(2)(4\text{-CBT})}$, 1.4×10^7 units in 1 mL EtOH) were added to the beads (10 mg, 1 mL in DMF). The mixture was reacted for 1 h at

25 °C, and washed with EtOH and DMF several times. Finally, after the conjugation of N_{leu}, 1 mL of micro-encoders which contain 3 holes and 4-BBT (micro-encoders$_{(3)(4\text{-BBT})}$, 7 x 10^6 units in 1 mL EtOH) were added to the beads (10 mg, 1 mL in DMF). The mixture was reacted for 1 h at 25 °C, and washed with EtOH and DMF several times.

After the peptoid synthesis and encoding processes were completed, beads containing penpapeptoid (10 mg) and bare beads as a control (10 mg) were treated with 2 mL of 5 % BSA solution in 10 mM PBS (pH 7.4) for 30 min at 25 °C. Then the beads were washed with PBS for several times. Then, 2 mL of streptavidin-FITC (20 μg/mL in PBS) was added to the beads (10 mg) and reacted for 1 h at 25 °C. Then, the beads were washed with PBS and transferred to a glass slide. The confocal microscope image was obtained from the beads which bind to streptavidin-FITC with 488 nm laser excitation. Then, the SERS intensity maps from the micro-encoders on the beads were obtained, using point-by-point SERS mapping with a 1 μm step size using a 660 nm laser at a power of 5 mW for 1 s. ESI-MS analysis was conducted after the

cleavage of pentapeptoid from the beads by irradiating 365 nm UV light for 30 min at the beads (10 mg, 3 mL in MC).

2. Results and Discussion

2.1. Preparation of Ag NPs-assembled Silica Micro-disks

The silica-coated Ag NPs-assembled silica micro-disks (micro-encoders) were fabricated to encode the sequence and type of peptoid side chain (Fig. 25). Three types of micro-encoders were used, which can be distinguished by the number of holes inside micro-encoders. Sequence of peptoid side chain can be identified by the number of holes. The type of peptoid side chain can be identified by the SERS signals from micro-encoders.

Silica micro-disks were synthesized by photolithography process (Fig. 26). The SiO_2 layer with the thickness about 1 μm was built uniformly on the surface of silicon wafer through wet oxidation process. Then, the designated region on SiO_2 layer was etched according to the shape of photoresist layer, and can be distinguished by the number of holes. The resulting silica micro-disks also have holes whose size is about 1 μm. As the last stage of photolithography process, the silica micro-disks were released from the silicon wafer by treating with aqueous tetramethyl

ammonium hydroxide (TMAH) solution (20%), and collected by centrifugation.

For additional functionalization of silica micro-disks, thiol groups were introduced onto the bare silica micro-disks by reacting with 3-mercaptopropyltrimethoxysilane (MPTS). Ag^{+} ions were reduced on the surface of thiol treated silica micro-disks utilizing the interaction between the thiol groups of MPTS and the silver ions, affording silver NPs. Then, the Ag NPs-assembled silica micro-disks were treated with three kinds of Raman reporter molecules; 4-FBT, 4-CBT, and 4-BBT.

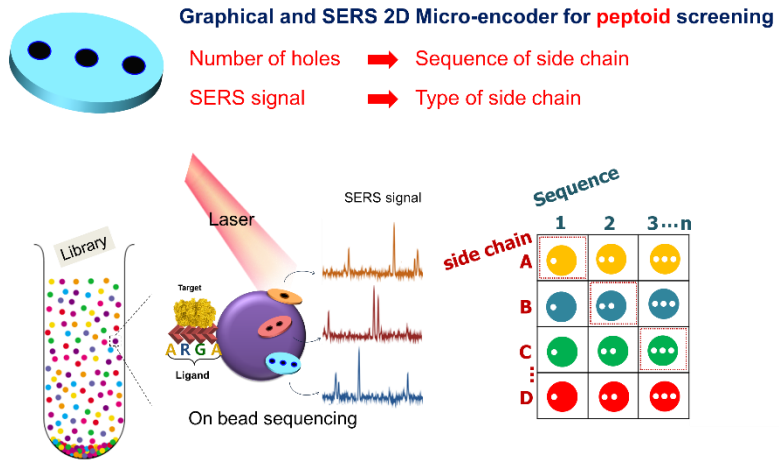

Figure 25. The schematic illustration of graphical and SERS two-dimensional encoding using micro-encoders.

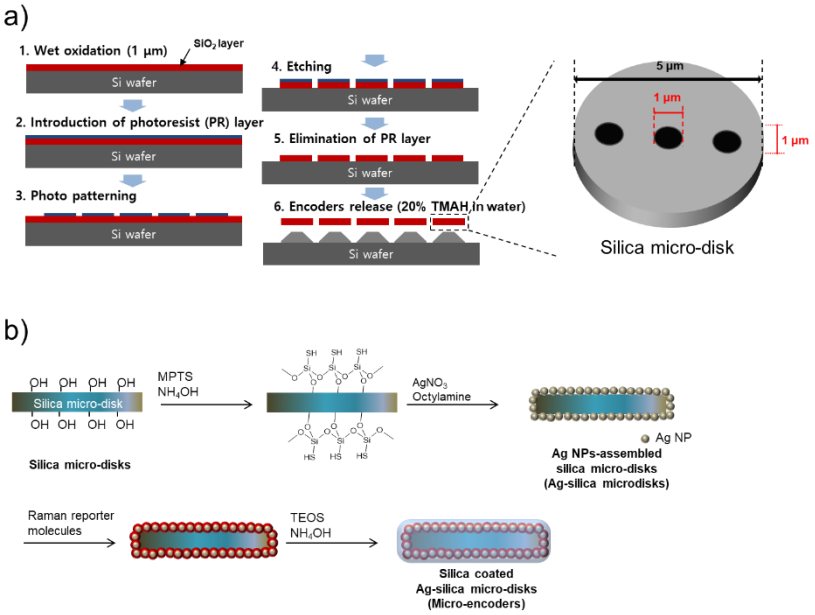

Figure 26. Overall scheme for the fabrication of micro-encoders. a) Photolithographic process for the fabrication of silica micro-disks, and b) surface modification of silica micro-disks.

2.2. Characterization of Silica Micro-disks and Ag NPs-assembled Silica Micro-disks

The scanning electron microscopy (SEM) images of silica micro-disks were shown in Fig. 27. Three types of silica micro-disks which are 5 μm in size, were released from silicon wafer. By the number of holes located in the center of silica micro-disk, the type of silica micro-disk could be distinguished visually by SEM image. After Ag^+ ion reduction process, Ag NPs-assembled silica micro-disks were prepared and analyzed by SEM images and EDX analysis as shown in Fig. 28. Compared to the smooth surface of bare silica micro-disk, rough surface could be identified by magnified SEM images. Also, peak at 2.983 eV that corresponds to Lα peak of Ag was observed from the Ag NPs-assembled silica micro-disk, which could not be observed in bare silica micro-disk. The formation of Ag NPs could be additionally confirmed by the chemical compositions based on EDX analysis as shown in Table 1, which reveals that atomic ratio of Ag in Ag NPs-assembled silica micro-disk is about 6.74%. These results proves the

formation of Ag NPs on the surface of silica micro-disks. Also, the number of holes in the Ag NPs-assembled silica micro-disks could be still identified.

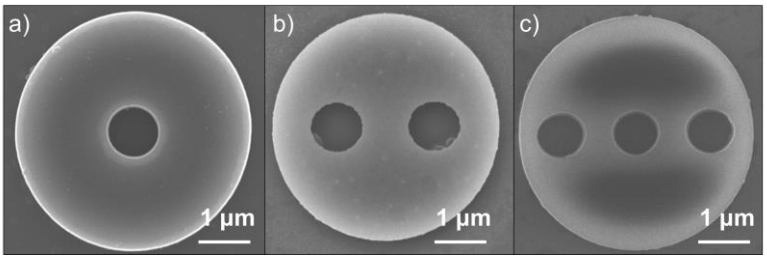

Figure 27. The SEM images of silica micro-disks with a) 1, b) 2, and c) 3 holes.

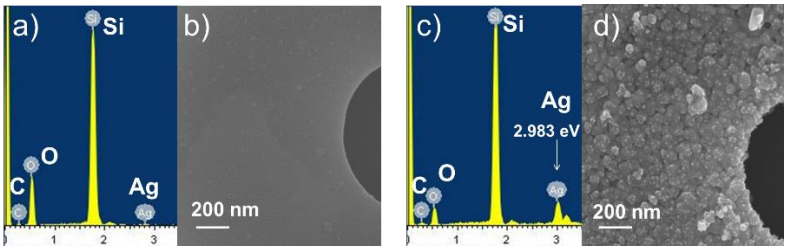

Figure 28. The EDX analysis of a) bare silica micro-disks and c) Ag NPs-assembled silica micro-disks with their corresponding SEM images b) and d).

Table 1. Chemical compositions of Ag in bare silica micro-disks and Ag NPs-assembled silica micro-disks

Element	Silica micro-disks	Ag NPs-assembled silica micro-disks
Ag (L) Atomic %	0.02	5.74

2.3. Optimization of Ag NPs Formation on Silica Micro-disks

In order to find out the optimal conditions for the formation of Ag NPs, the concentrations of $AgNO_3$ and octylamine (0.1, 0.25, 0.5, 0.75, 1 mM) were varied and 4-FBT as a Raman reporter molecule was successively treated to the resulting silica micro-disks. Then, SEM images and SERS intensity map of each silica micro-disk were obtained using point-by-point mapping with a 1 μm step size using a 532 nm laser at a power of 0.06 mW (Fig. 29). When 0.1 mM of $AgNO_3$ and octylamine were treated, Ag NPs could be rarely observed on the surface of silica micro-disks, as shown in Fig. 29a. As expected, SERS signal could not be obtained from the silica micro-disks treated with 0.1 mM of $AgNO_3$ and octylamine. However, when the concentrations of $AgNO_3$ and octylamine were higher than 0.5 mM, SERS signal could be obtained from the entire region of the silica micro-disk as shown in SERS map (Fig. 29c). As evaluated by the height of the 1075 cm^{-1} peak (the highest peak in the spectrum of 4-FBT) in the

spectrum, the SERS intensities increased almost linearly when the concentrations of $AgNO_3$ and octylamine increased, as shown in Fig. 29f. Because the excessive Ag coating should be avoided, which would result in the disapperance of holes in silica micro-disks, 0.5 mM was decided as the optimal condition for the formation of Ag NPs on silica micro-disks.

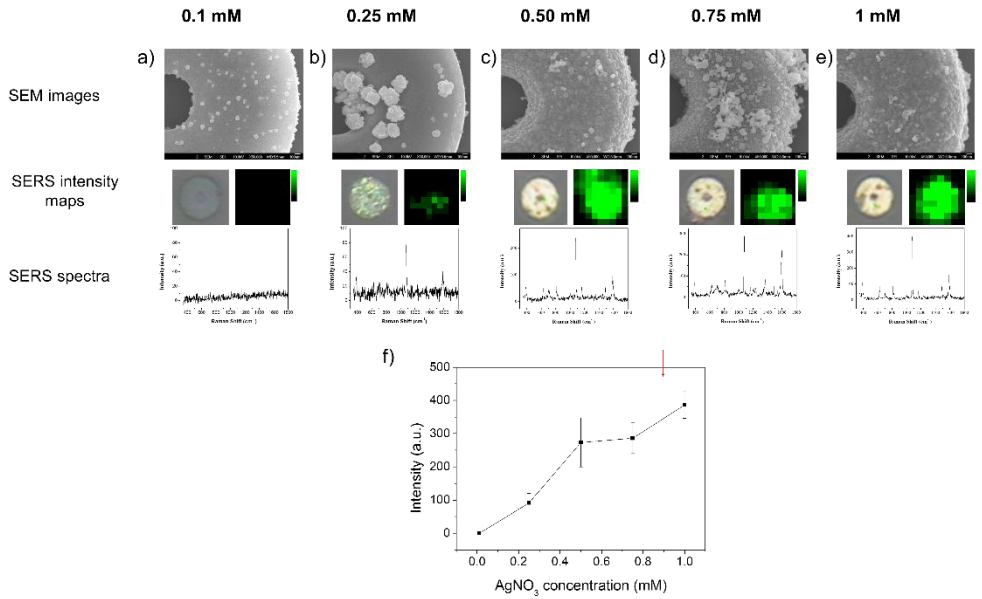

Figure 29. The SEM images, SERS intensity maps, and SERS spectra of Ag NPs-assembled silica micro-disks vs. the concentrations of $AgNO_3$ and octylamine during formation of Ag NPs. The concentrations of $AgNO_3$ and octylamine were a) 0.1 mM, b) 0.25 mM, c) 0.5 mM, d) 0.75 mM, and e) 1 mM. f) SERS intensities of Ag NPs-assembled silica micro-disks treated with different concentrations of $AgNO_3$ and octylamine during Ag^+ ion reduction process.

2.4. Silica Coating on Ag NPs-assembled Silica Micro-disks and Preparation of Micro-encoders

Silica layer was coated on the Ag NPs-assembled silica micro-disks to retain stability during peptoid ligands synthesis on TG bead. As shown in Fig. 30a, the shape of the resulting micro-encoders could be clearly confirmed, if excessive silica coating was avoided, which can result in the disappearance of the holes in the micro-encoders. Nine types of micro-encoders were prepared, three types of graphical codings and three kinds of SERS codings. The SERS intensity maps were presented in Fig. 30b. Thus, micro-encoder library for on-bead identification of peptoid ligands was successfully prepared.

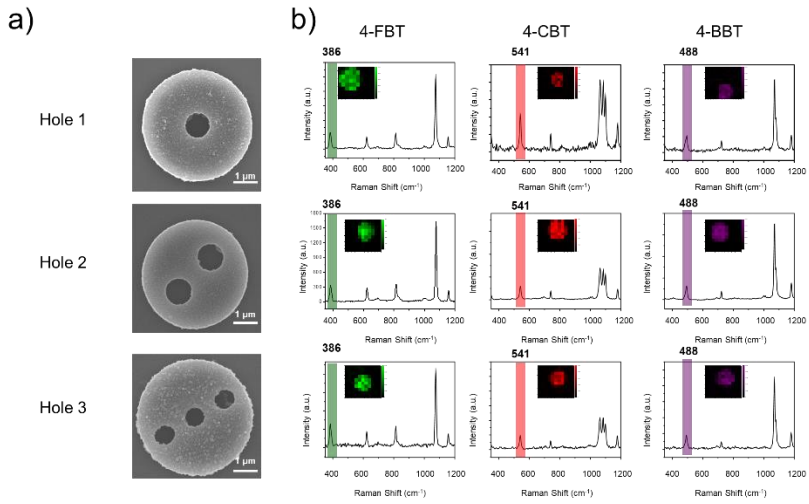

Figure 30. SEM images and SERS spectra of micro-encoders. a) The SEM images of micro-encoders. b) SERS spectra of micro-encoders treated with three kinds of Raman reporter molecules; 4-FBT, 4-CBT, and 4-BBT. The inset shows SERS intensity maps of micro-encoders.

2.5. Tagging TG Beads by Embedding Micro-encoders

The peptoid sequence can be encoded by the absorption of micro-encoders on TentaGel (TG) beads after each peptoid coupling reaction on TG beads. Sufficient amount of micro-encoders should remain stable on TG beads during peptoid synthesis in order to obtain the sequence information from the micro-encoders effectively after on-bead assay. Thus, the relationship between the amount of added micro-encoders and the amount of embedded micro-encoders was investigated. The number of added micro-encoders per bead was controlled from 10 to 800 and the number of embedded micro-encoders per bead was counted by SEM images (Fig. 31). The average number of embedded micro-encoders per bead was increased depending on the number of added micro-encoders per bead, as presented in Table 2. Based on this result, we could confirm that ~ 50% of added micro-encoders were embedded on bare TG beads. The micro-encoders were also embedded to the photolabile linker (PLL)-coupled TG beads, in order to check the stability of the interaction between the micro-

encoders and the PLL-coupled TG beads during actual peptoid synthesis process. However, the average number of embedded micro-encoders per bead was decreased to ~10% of added amounts as shown in Fig. 32 and Table 3. It is probably due to the reduced number of functional groups after PLL modification on the beads. After embedding micro-encoders on the PLL-coupled TG beads, SEM images and SERS spectra of micro-encoders on beads were obtained (Fig. 33). Even though the beads were treated with *N,N'*-diisopropylcarbodiimide (DIC) or incubated with MC for 30 min, average number of micro-encoders per bead or SERS intensities of the micro-encoders did not decreased. Based on these results, we confirmed that the micro-encoders are stable to be used on TG beads during peptoid synthesis process.

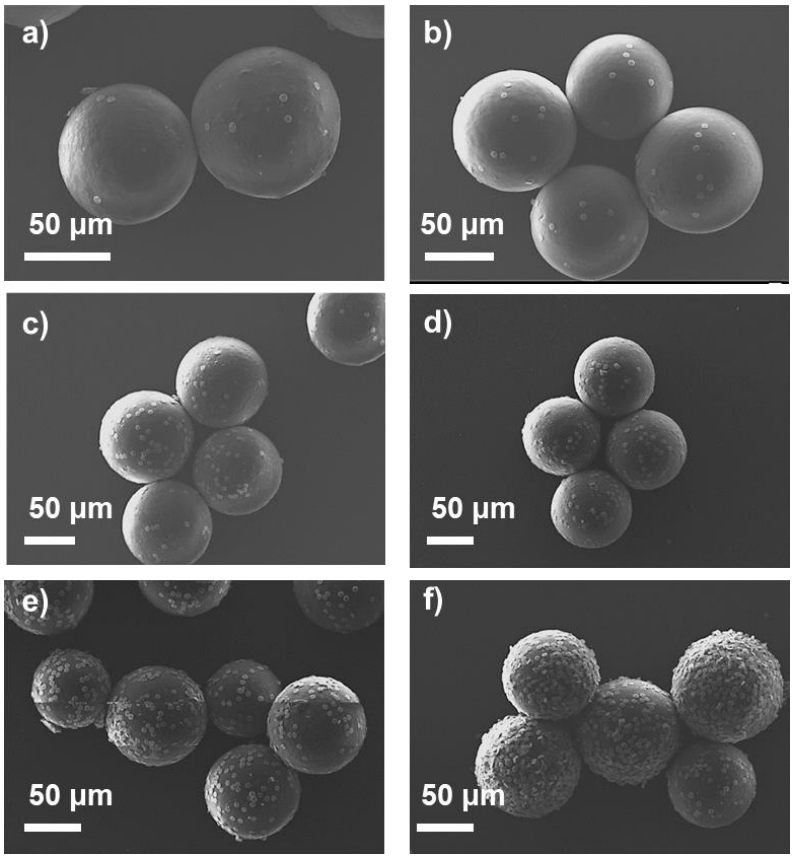

Figure 31. The SEM images of micro-encoders embedded on TG beads. The number of added micro-encoders per bead was a) 10, b) 50, c) 100, d) 200, e) 400, and f) 800.

Table 2. The average number of embedded micro-encoders per bead when the number of added micro-encoders per bead was controlled from 10 to 800

The number of added micro-encoders per bead	10	50	100	200	400	800
Average number of embedded micro-encoders per bead	8	20	64	90	238	424

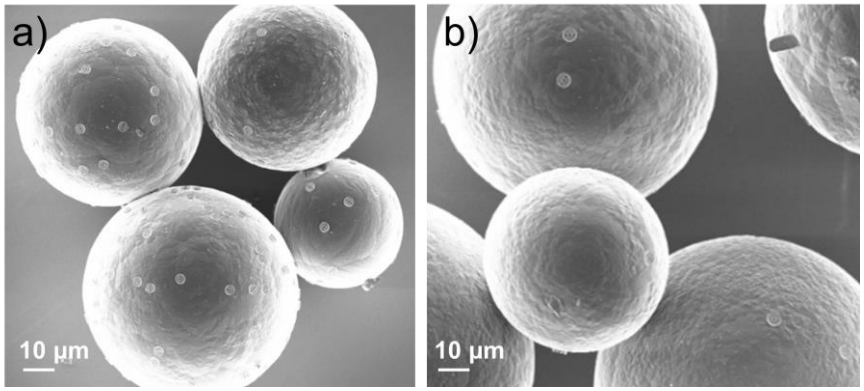

Figure 32. The SEM images of micro-encoders embedded on a) bare beads and b) PLL modified beads. The number of added micro-encoders per bead was 50.

Table 3. The average number of embedded micro-encoders per bare bead and PLL modified bead[a]

	Bare bead	PLL modified bead
Average number of embedded micro-encoders per bead	26	4

[a]The number of added micro-encoders per bead was 50

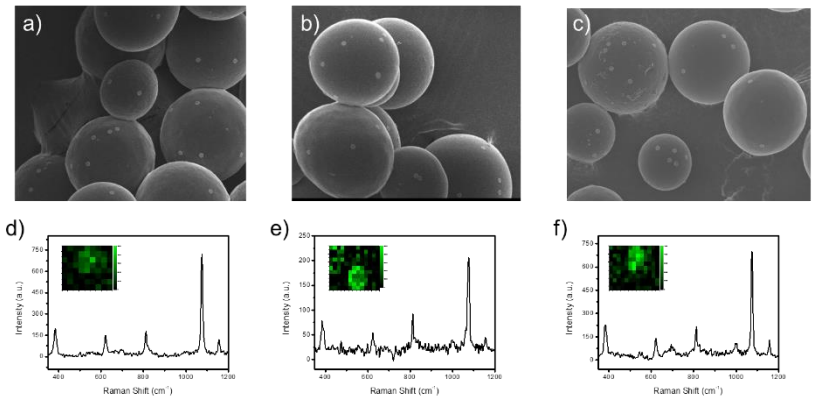

Figure 33. The SEM images of micro-encoders embedded on PLL modified beads, a) before treatment, b) after treating with DIC, and c) after incubating with MC for 30 min. The SERS spectra of micro-encoders embedded on PLL modified beads, d) before treatment, e) after treating with DIC, and f) after incubating with MC for 30 min. The inset shows SERS intensity maps of micro-encoders on beads.

2.6. Optimization of Peptoid Coupling Reaction on TG Beads

The solid-phase peptoid synthesis includes alternate reaction of bromoacetic acid and primary amines on TG beads, as shown in Fig. 34. Bromoacetic acid, after activation with DIC, is reacted with amine functional groups on TG beads. Then, primary amines are treated to the TG beads, and the type of peptoid side chain is determined by the substituent of the primary amine. Because the amount of micro-encoders embedded on TG beads can be affected by peptoid coupling reaction, the conditions of peptoid coupling reaction were optimized in order to minimize desorption of micro-encoders. When the micro-encoders were embedded on TG beads, the average number of embedded micro-encoders per bead was adjusted as 50 before testing. These beads were reacted with bromoacetic acid and primary amines at various reaction conditions, and the average number of embedded micro-encoders left per bead was investigated after each coupling reaction.

First, various amounts of bromoacetic acid (5, 10, and 20 equivalent of the amine functional groups on TG beads) were

treated to the beads. The amount of DIC was fixed as 20 equivalent of the amine functional groups on TG beads. The reaction was confirmed by acetaldehyde/chrolanil test, and the amount of micro-encoders embedded on TG beads was counted by SEM images (Fig. 35). As shown in Table 4, maximum amounts of micro-encoders were left on TG beads when 5 equivalent of bromoacetic acid was used. However, acetaldehyde/chrolanil test showed that there were unreacted amine left on TG beads and the reaction was not proceeded completely. Thus, 10 equivalent of bromoacetic acid was determined to be the optimal condition for maintaining maximal amount of micro-encoders on TG beads.

Second, after the beads were reacted with 10 equivalent of bromoacetic acid, various amounts of 2-methoxyethylamine (N_{mea}, 10, 20, and 50 equivalent of the amine groups on TG beads) were treated on the beads. The reaction was also followed by acetaldehyde/chrolanil test, and the amount of micro-encoders embedded on TG beads was counted by SEM images (Fig. 36). As presented in Table 5, when 10 equivalent of N_{mea} was treated, the largest amount of micro-encoders were left on TG beads and the

reaction was proceeded completely. Thus, 10 equivalent of primary amine was determined to be the optimal condition for peptoid coupling reaction. Furthermore, the number of micro-encoders per bead after the beads were reacted with optimal amount of bromoacetic acid and primary amine was 24, which means that about 50% of the micro-encoders remained on the beads during elongation of a single peptoid side chain.

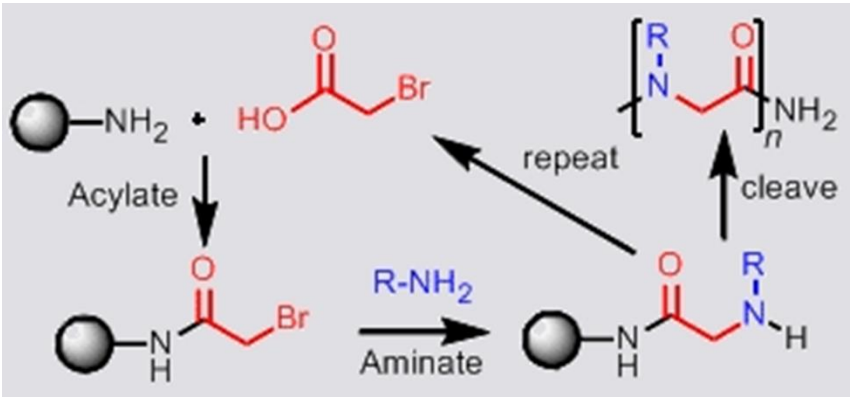

Figure 34. The scheme for solid-phase peptoid synthesis which is composed of alternate reactions of bromoacetic acid and primary amine on beads.

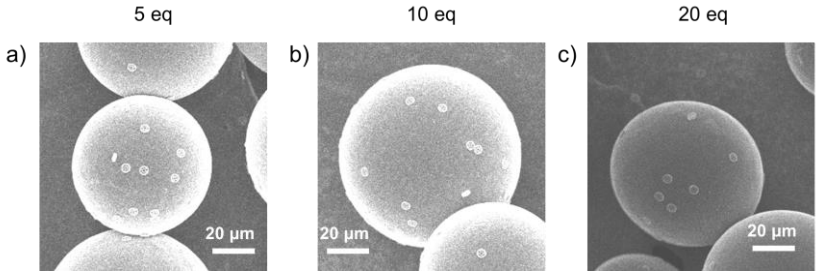

Figure 35. The SEM images of micro-encoders embedded on TG beads after treating with a) 5, b) 10, and c) 20 equivalent of bromoacetic acid.

Table 4. The average number of micro-encoders embedded on TG bead and acetaldehyde/chloranil test results after treating with various amount of bromoacetic acid

Amount of treated bromoacetic acid	5 eq	10 eq	20 eq
Average number of embedded micro-encoders per bead	20	16	12
Acetaldehyde/chloranil test results	positive	negative	negative

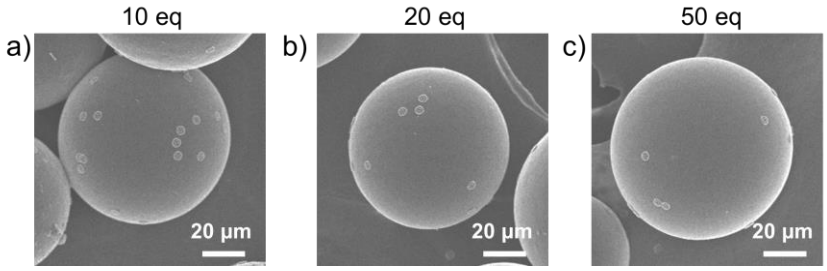

Figure 36. The SEM images of micro-encoders embedded on TG bead after treating with a) 10, b) 20, and c) 50 equivalent of N_{mea}.

Table 5. The average number of micro-encoders embedded on TG bead and acetaldehyde/chloranil test results after treating with various amount of N_{mea}

Amount of treated amine	10 eq	20 eq	50 eq
Average number of embedded micro-encoders per bead	24	16	10
Acetaldehyde/chloranil test results	positive	positive	positive

2.7. Encoding Peptoid Sequence on TG Beads Using Micro-encoders

To confirm the usefulness of micro-encoders in encoding peptoid sequence, synthesis of peptoid sequence, encoding, and decoding on TG beads were performed. Streptavidin-conjugated fluorescein isothiocyanate (streptavidin-FITC) was utilized as a target for peptioid ligand and the binding event was confirmed by the fluorescent signal. The previously reported sequence which can bind to streptavidin is composed of 2-methoxyethylamine (N_{mea}), *N*-(3-aminopropyl)-2-pyrrolidinone (N_{app}), 1-naphtylmethylamine (N_{nap}), piperonylamine (N_{pip}), and isobutylamine (N_{leu})[89]. Based on this, the penta-peptoid (N_{mea} - N_{app} - N_{nap} - N_{pip} - N_{leu}) was synthesized and the last three sequences were encoded using micro-encoders. That is, N_{nap}, N_{pip}, and N_{leu} were encoded using micro-encoders with 1 hole and the SERS signal of 4-FBT (micro-encoders$_{(1)(4\text{-FBT})}$), micro-encoders with 2 holes and the SERS signal of 4-CBT (micro-encoders$_{(2)(4\text{-CBT})}$), and micro-encoders with 3 holes and the SERS signal of 4-BBT (micro-encoders$_{(3)(4\text{-}}$

$_{BBT)}$), respectively (Fig. 37).

As discussed in Section 2.6, the amount of micro-encoders on TG beads was decreased to 50% during elongation of the peptoid sequence on TG beads. Therefore, the amount of micro-encoders$_{(1)(4\text{-}FBT)}$ which correspond to N_{nap} might decrease to 25%, when the pentapeptoid synthesis is completed. It is because the beads should undergo peptoid coupling reactions twice. Similarly, the amount of micro-encoders$_{(2)(4\text{-}CBT)}$ is expected to decrease to 50%. Thus, the added ratio of the amount of micro-encoders during each coupling reatcion was determined to be 4:2:1 to adjust the final embedded amount of each micro-encoders. The SEM images upon embedding each micro-encoders are shown in Fig. 38. As shown in Fig. 38c, three types of micro-encoders were evenly distributed on the beads after pentapeptoid synthesis.

After the synthesis of pentapeptoid and encoding processes, both the pentapeptoid coupled beads and the bare beads as a control were treated with 5% bovine serum albumin (BSA) in phosphate buffered saline (PBS, 10 mM, pH 7.4) to prevent non-specific protein binding. The beads were then treated with streptavidin-

FITC. As shown in Fig. 39a and Fig. 39b, the binding event of the pentapeptoid coupled bead and streptavidin could be confirmed by the florescence of FITC, while the control beads did not bind to streptavidin. The SERS intensity maps from the micro-encoders on streptavidin bound beads were obtained, as shown in Fig. 39c. The SERS spectra of 4-FBT, 4-CBT, and 4-BBT could be obtained from each of the micro-encoders$_{(1)(4\text{-FBT})}$, the micro-encoders$_{(2)(4\text{-CBT})}$, and the micro-encoders$_{(3)(4\text{-BBT})}$, respectively, showing that the encoded peptoid sequence can be unambiguously identified based on the graphical pattern and the SERS signal of the micro-encoders. To confirm that encoding was correctly proceeded, electrospray ionization mass spectrometry (ESI-MS) analysis of the released pentapeptoid was conducted after irradiating 365 nm UV laser at the beads. As shown in Fig. 40, the mass spectroscopic analysis of the pentapeptoid indicated that the pentapeptoid was successfully synthesized and accurately identified using the micro-encoders. Based on these results, we can conclude that effective encoding and decoding can be performed using the micro-encoders on TG bead after the peptoid sequences are bound to a target.

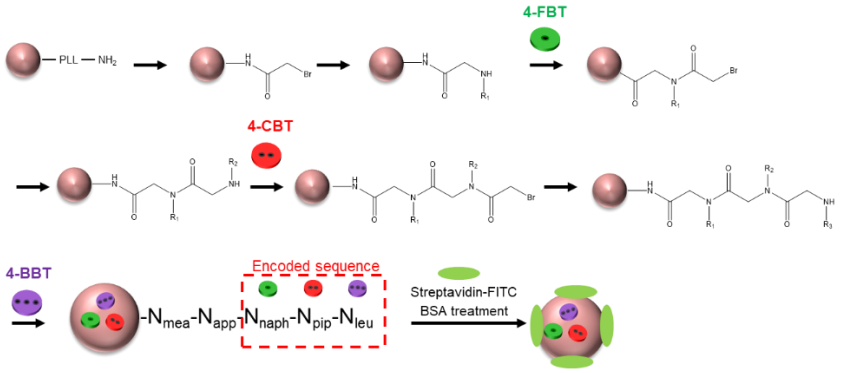

Figure 37. The scheme for encoding process using three types of micro-encoders for the last three peptoid sequences.

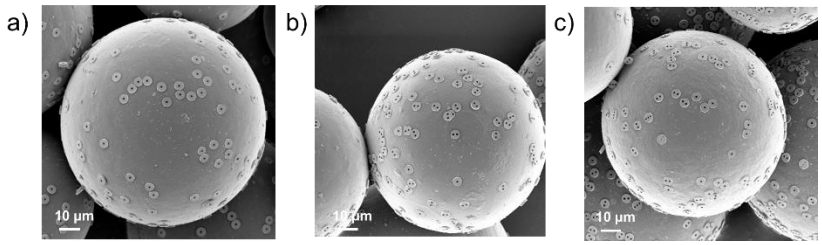

Figure 38. The SEM images of TG beads after embedding a) micro-encoders$_{(1)(4\text{-FBT})}$, b) micro-encoders$_{(2)(4\text{-CBT})}$, and c) micro-encoders$_{(3)(4\text{-BBT})}$ during pentapeptoid synthesis.

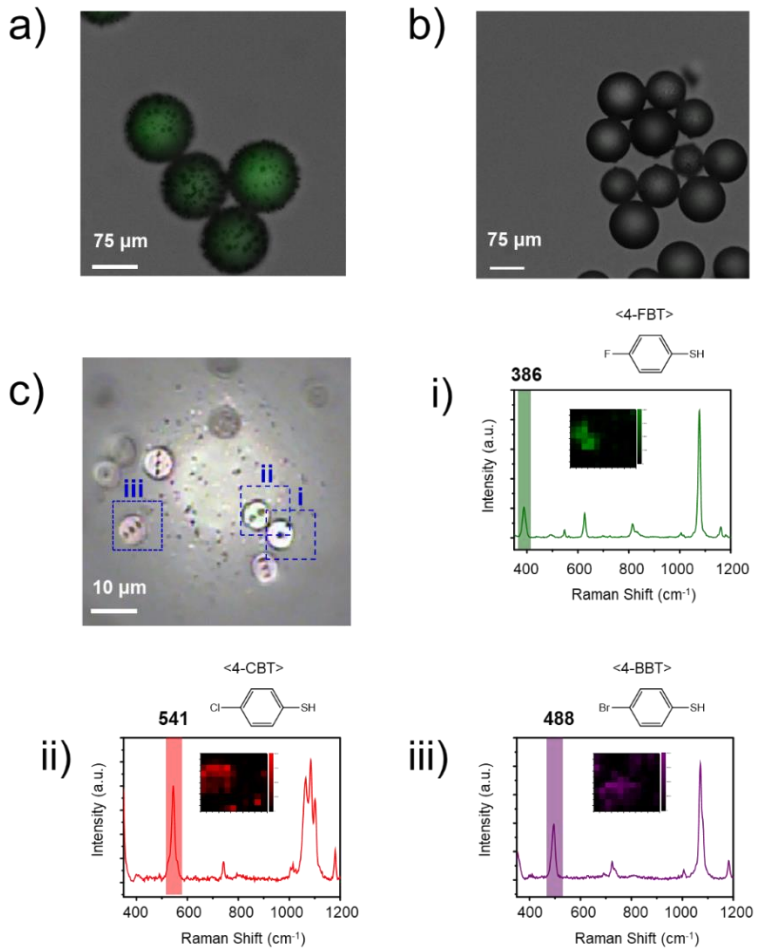

Figure 39. The confocal microscope image of a) streptavidin bound TG beads and b) control beads. c) Optical image of micro-encoders on streptavidin bound TG beads and SERS spectra of i) micro-encoders$_{(1)(4\text{-FBT})}$, ii) micro-encoders$_{(2)(4\text{-CBT})}$, and iii) micro-encoders$_{(3)(4\text{-BBT})}$. The insets show SERS intensity maps of micro-encoders which correspond to the region in optical image.

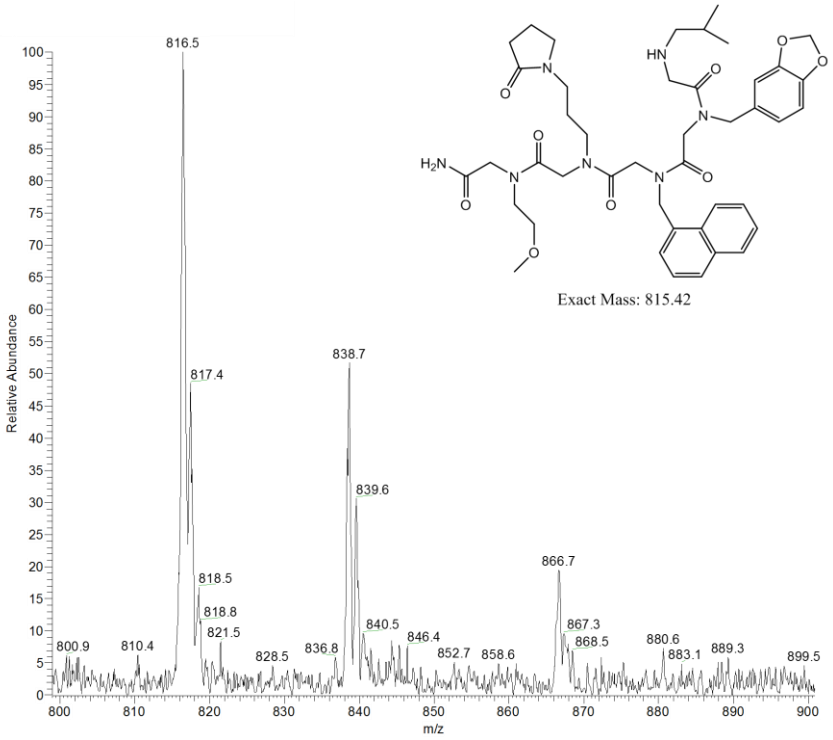

Figure 40. ESI-MS spectrum of pentapeptoid (N_{mea} - N_{app} - N_{nap} - N_{pip} - N_{leu}).

3. Conclusion

A simple and efficient encoding method for peptoid library on bead was developed by using two-dimensional graphical and SERS micro-encoder. Holes are located on the micro-encoders were used to encode the sequence of peptoid side chain, and the SERS signals from the Ag NPs on the micro-encoders were used to encode the type of side chain. The micro-encoders were successfully prepared by photolithography process and Ag NPs were assembled on the surface of silica layer for a SERS substrate. Nine types of micro-encoders were prepared, which can be distinguished by three types of graphical pattern and three kinds of SERS signals. For embedding appropriate amount of micro-encoders on TG beads during peptoid synthesis, the number of added micro-encoders were optimized during the peptoid synthesis cycles. Also, the conditions for peptoid coupling reactions were optimized for keeping maximal amount of micro-encoders on TG beads. The pentapeptoid which can bind to streptavidin was synthesized on TG beads and encoded sucessfully using the micro-

encoders. After confirming the binding event of peptoid conjugated TG beads with streptavidin-FITC by confocal microscope image, the graphical pattern and SERS signal of micro-encoders on TG beads were identified. Based on these results, we conclude that micro-encoders can be effectively utilized to encode peptoid ligands or small organic molecules on beads.

References

1. M. Fleischmann, P. J. Hendra and A. J. McQuillan, *Chemical Physics Letters*, 1974, **26**, 163-166.
2. D. L. Jeanmaire and R. P. Van Duyne, *Journal of Electroanalytical Chemistry and Interfacial Electrochemistry*, 1977, **84**, 1-20.
3. T.-Y. Chan, T.-Y. Liu, K.-S. Wang, K.-T. Tsai, Z.-X. Chen, Y.-C. Chang, Y.-Q. Tseng, C.-H. Wang, J.-K. Wang and Y.-L. Wang, *Nanoscale Research Letters*, 2017, **12**, 344.
4. D. van Lierop, K. Faulds and D. Graham, *Analytical chemistry*, 2011, **83**, 5817-5821.
5. J. Yang, Y. Cui, S. Zong, R. Zhang, C. Song and Z. Wang, *Molecular pharmaceutics*, 2012, **9**, 842-849.
6. H. Xu, J. Aizpurua, M. Käll and P. Apell, *Physical Review E*, 2000, **62**, 4318.
7. J. P. Kottmann and O. J. Martin, *Optics Letters*, 2001, **26**, 1096-1098.
8. A. Campion and P. Kambhampati, *Chemical Society Reviews*, 1998, **27**, 241-250.
9. T. Vo-Dinh, *TrAC Trends in Analytical Chemistry*, 1998, **17**, 557-582.
10. C. L. Haynes and R. P. Van Duyne, *The Journal of Physical Chemistry B*, 2003, **107**, 7426-7433.

11. A. D. McFarland, M. A. Young, J. A. Dieringer and R. P. Van Duyne, *The Journal of Physical Chemistry B*, 2005, **109**, 11279-11285.
12. P. L. Stiles, J. A. Dieringer, N. C. Shah and R. P. Van Duyne, *Annu. Rev. Anal. Chem.*, 2008, **1**, 601-626.
13. Y. Zheng, T. Thai, P. Reineck, L. Qiu, Y. Guo and U. Bach, *Advanced Functional Materials*, 2013, **23**, 1519-1526.
14. M. J. Banholzer, J. E. Millstone, L. Qin and C. A. Mirkin, *Chemical Society Reviews*, 2008, **37**, 885-897.
15. A. F. McCabe, C. Eliasson, R. A. Prasath, A. Hernandez-Santana, L. Stevenson, I. Apple, P. A. Cormack, D. Graham, W. E. Smith and P. Corish, *Faraday discussions*, 2006, **132**, 303-308.
16. H. Chon, S. Lee, S. W. Son, C. H. Oh and J. Choo, *Analytical chemistry*, 2009, **81**, 3029-3034.
17. S. Lee, H. Chon, M. Lee, J. Choo, S. Y. Shin, Y. H. Lee, S. W. Son and C. H. Oh, *Biosensors and Bioelectronics*, 2009, **24**, 2260-2263.
18. M. Sanles-Sobrido, W. Exner, L. Rodríguez-Lorenzo, B. Rodríguez-González, M. A. Correa-Duarte, R. A. Álvarez-Puebla and L. M. Liz-Marzán, *Journal of the American Chemical Society*, 2009, **131**, 2699-2705.
19. B. Goris, L. Polavarapu, S. Bals, G. Van Tendeloo and L. M. Liz-Marzán, *Nano letters*, 2014, **14**, 3220-3226.

20. L. Polavarapu, D. Zanaga, T. Altantzis, S. Rodal-Cedeira, I. Pastoriza-Santos, J. Pérez-Juste, S. Bals and L. M. Liz-Marzán, *Journal of the American Chemical Society*, 2016, **138**, 11453-11456.
21. D. H. Jeong, Y. X. Zhang and M. Moskovits, *The Journal of Physical Chemistry B*, 2004, **108**, 12724-12728.
22. S. J. Lee, A. R. Morrill and M. Moskovits, *Journal of the american chemical society*, 2006, **128**, 2200-2201.
23. J. F. Li, Y. F. Huang, Y. Ding, Z. L. Yang, S. B. Li, X. S. Zhou, F. R. Fan, W. Zhang, Z. Y. Zhou and B. Ren, *nature*, 2010, **464**, 392-395.
24. K. Kwon, K. Y. Lee, Y. W. Lee, M. Kim, J. Heo, S. J. Ahn and S. W. Han, *The Journal of Physical Chemistry C*, 2007, **111**, 1161-1165.
25. J. M. McLellan, Z.-Y. Li, A. R. Siekkinen and Y. Xia, *Nano letters*, 2007, **7**, 1013-1017.
26. W. Li, P. H. Camargo, L. Au, Q. Zhang, M. Rycenga and Y. Xia, *Angewandte Chemie International Edition*, 2010, **49**, 164-168.
27. Y. Lu, G. L. Liu, J. Kim, Y. X. Mejia and L. P. Lee, *Nano letters*, 2005, **5**, 119-124.
28. C. L. Haynes, A. D. McFarland, L. Zhao, R. P. Van Duyne, G. C. Schatz, L. Gunnarsson, J. Prikulis, B. Kasemo and M. Käll, *The Journal of Physical Chemistry B*, 2003, **107**, 7337-7342.
29. J. Xie, Q. Zhang, J. Y. Lee and D. I. Wang, *ACS*

nano, 2008, **2**, 2473-2480.
30. C. G. Khoury and T. Vo-Dinh, *The Journal of Physical Chemistry C*, 2008, **112**, 18849-18859.
31. B. Nikoobakht, J. Wang and M. A. El-Sayed, *Chemical Physics Letters*, 2002, **366**, 17-23.
32. Y. Wang, K. Lee and J. Irudayaraj, *Chemical Communications*, 2010, **46**, 613-615.
33. G. Hongyan, L. Linghui, W. Chao, P. Jiangao and H. Jiawen, *Acta Chimica Sinica*, 2009, **67**, 1603-1608.
34. L. Qin, M. J. Banholzer, J. E. Millstone and C. A. Mirkin, *Nano letters*, 2007, **7**, 3849-3853.
35. C. Wang, Y. Chen, T. Wang, Z. Ma and Z. Su, *Advanced Functional Materials*, 2008, **18**, 355-361.
36. J.-H. Kim, J.-S. Kim, H. Choi, S.-M. Lee, B.-H. Jun, K.-N. Yu, E. Kuk, Y.-K. Kim, D. H. Jeong and M.-H. Cho, *Nanomedicine: Nanotechnology, Biology and Medicine*, 2006, **2**, 317-318.
37. H. Kang, J.-K. Yang, M. S. Noh, A. Jo, S. Jeong, M. Lee, S. Lee, H. Chang, H. Lee and S.-J. Jeon, *Journal of Materials Chemistry B*, 2014, **2**, 4415-4421.
38. M. S. Noh, B.-H. Jun, S. Kim, H. Kang, M.-A. Woo, A. Minai-Tehrani, J.-E. Kim, J. Kim, J. Park and H.-T. Lim, *Biomaterials*, 2009, **30**, 3915-3925.
39. M.-A. Woo, S.-M. Lee, G. Kim, J. Baek, M. S. Noh, J. E. Kim, S. J. Park, A. Minai-Tehrani, S.-

C. Park and Y. T. Seo, *Analytical chemistry*, 2008, **81**, 1008-1015.
40. J. R. Anema, J.-F. Li, Z.-L. Yang, B. Ren and Z.-Q. Tian, *Annual Review of Analytical Chemistry*, 2011, **4**, 129-150.
41. K. Kneipp, H. Kneipp, V. B. Kartha, R. Manoharan, G. Deinum, I. Itzkan, R. R. Dasari and M. S. Feld, *Physical Review E*, 1998, **57**, R6281.
42. C. R. Yonzon, C. L. Haynes, X. Zhang, J. T. Walsh and R. P. Van Duyne, *Analytical Chemistry*, 2004, **76**, 78-85.
43. P. D. Bao, T. Q. Huang, X. M. Liu and T. Q. Wu, *Journal of Raman Spectroscopy*, 2001, **32**, 227-230.
44. G. Yao, L. Wang, Y. Wu, J. Smith, J. Xu, W. Zhao, E. Lee and W. Tan, *Analytical and Bioanalytical Chemistry*, 2006, **385**, 518-524.
45. I. L. Medintz, H. T. Uyeda, E. R. Goldman and H. Mattoussi, *Nature materials*, 2005, **4**, 435-446.
46. X. Michalet, F. Pinaud, L. Bentolila, J. Tsay, S. Doose, J. Li, G. Sundaresan, A. Wu, S. Gambhir and S. Weiss, *science*, 2005, **307**, 538-544.
47. R. K. Jain and M. Stroh, *Nature biotechnology*, 2004, **22**, 959-961.
48. K. Kneipp, Y. Wang, H. Kneipp, L. T. Perelman, I. Itzkan, R. R. Dasari and M. S. Feld, *Physical review letters*, 1997, **78**, 1667.
49. S. Nie and S. R. Emory, *science*, 1997, **275**,

1102-1106.
50. J. A. Dougan and K. Faulds, *Analyst*, 2012, **137**, 545-554.
51. R. Costi, A. E. Saunders and U. Banin, *Angewandte Chemie International Edition*, 2010, **49**, 4878-4897.
52. K. N. Yu, S.-M. Lee, J. Y. Han, H. Park, M.-A. Woo, M. S. Noh, S.-K. Hwang, J.-T. Kwon, H. Jin and Y.-K. Kim, *Bioconjugate chemistry*, 2007, **18**, 1155-1162.
53. M. H. Shin, W. Hong, Y. Sa, L. Chen, Y.-J. Jung, X. Wang, B. Zhao and Y. M. Jung, *Vibrational Spectroscopy*, 2014, **72**, 44-49.
54. K. Yang, Y. Hu and N. Dong, *Biosensors and Bioelectronics*, 2016, **80**, 373-377.
55. M. V. Yigit, L. Zhu, M. A. Ifediba, Y. Zhang, K. Carr, A. Moore and Z. Medarova, *ACS nano*, 2010, **5**, 1056-1066.
56. T. Zhou, B. Wu and D. Xing, *Journal of Materials Chemistry*, 2012, **22**, 470-477.
57. Y. Han, S.-l. Lei, J.-h. Lu, Y. He, Z.-w. Chen, L. Ren and X. Zhou, *Materials Science and Engineering: C*, 2016, **64**, 199-207.
58. U. Jeong, X. Teng, Y. Wang, H. Yang and Y. Xia, *Advanced Materials*, 2007, **19**, 33-60.
59. C. Sun, J. S. Lee and M. Zhang, *Advanced drug delivery reviews*, 2008, **60**, 1252-1265.
60. A. S. Teja and P.-Y. Koh, *Progress in crystal growth and characterization of materials*, 2009,

55, 22-45.
61. S. Kyeong, C. Jeong, H. Kang, H.-J. Cho, S.-J. Park, J.-K. Yang, S. Kim, H.-M. Kim, B.-H. Jun and Y.-S. Lee, *PloS one*, 2015, **10**, e0143727.
62. Y. Pang, C. Wang, J. Wang, Z. Sun, R. Xiao and S. Wang, *Biosensors and Bioelectronics*, 2016, **79**, 574-580.
63. C. Wang, J. Wang, M. Li, X. Qu, K. Zhang, Z. Rong, R. Xiao and S. Wang, *Analyst*, 2016, **141**, 6226-6238.
64. A. Carrouée, E. Allard-Vannier, S. Même, F. Szeremeta, J.-C. Beloeil and I. Chourpa, *Analytical Chemistry*, 2015, **87**, 11233− 11241.
65. Z. Wang, S. Zong, H. Chen, C. Wang, S. Xu and Y. Cui, *Advanced healthcare materials*, 2014, **3**, 1889-1897.
66. A. D. Keefe, S. Pai and A. Ellington, *Nature reviews. Drug discovery*, 2010, **9**, 537.
67. X. Yang, N. Li and D. G. Gorenstein, *Expert opinion on drug discovery*, 2011, **6**, 75-87.
68. A. S. Culf and R. J. Ouellette, *Molecules*, 2010, **15**, 5282-5335.
69. S. Østergaard and A. Holm, *Molecular diversity*, 1997, **3**, 17-27.
70. L. A. Marcaurelle and P. H. Seeberger, *Current opinion in chemical biology*, 2002, **6**, 289-296.
71. A. R. Vaino and K. D. Janda, *Proceedings of the National Academy of Sciences*, 2000, **97**, 7692-7696.

72. M. C. Needels, D. G. Jones, E. H. Tate, G. L. Heinkel, L. M. Kochersperger, W. J. Dower, R. W. Barrett and M. A. Gallop, *Proceedings of the National Academy of Sciences*, 1993, **90**, 10700-10704.
73. S. Brenner and R. A. Lerner, *Proceedings of the National Academy of Sciences*, 1992, **89**, 5381-5383.
74. M. S. Shchepinov, R. Chalk and E. M. Southern, *Tetrahedron*, 2000, **56**, 2713-2724.
75. L. S. Simpson and T. Kodadek, *Tetrahedron letters*, 2012, **53**, 2341-2344.
76. R. Wilson, A. R. Cossins and D. G. Spiller, *Angewandte Chemie International Edition*, 2006, **45**, 6104-6117.
77. H. Fenniri, S. Chun, L. Ding, Y. Zyrianov and K. Hallenga, *Journal of the American Chemical Society*, 2003, **125**, 10546-10560.
78. K. Braeckmans, S. C. De Smedt, M. Leblans, R. Pauwels and J. Demeester, *Nature reviews. Drug discovery*, 2002, **1**, 447.
79. M. Han, X. Gao, J. Z. Su and S. Nie, *Nature biotechnology*, 2001, **19**, 631.
80. Y. Lai, S. Sun, T. He, S. Schlücker and Y. Wang, *Rsc Advances*, 2015, **5**, 13762-13767.
81. H. Kang, S. Jeong, Y. Koh, M. G. Cha, J.-K. Yang, S. Kyeong, J. Kim, S.-Y. Kwak, H.-J. Chang and H. Lee, *Scientific reports*, 2015, **5**.
82. M. L. Huang, D. Ehre, Q. Jiang, C. Hu, K.

Kirshenbaum and M. D. Ward, *Proceedings of the National Academy of Sciences*, 2012, **109**, 19922-19927.
83. W. Stöber, A. Fink and E. Bohn, *Journal of colloid and interface science*, 1968, **26**, 62-69.
84. C. Xu, K. Xu, H. Gu, R. Zheng, H. Liu, X. Zhang, Z. Guo and B. Xu, *Journal of the American Chemical Society*, 2004, **126**, 9938-9939.
85. H. Kang, J. Yim, S. Jeong, J.-K. Yang, S. Kyeong, S.-J. Jeon, J. Kim, K. D. Eom, H. Lee and H.-I. Kim, *ACS applied materials & interfaces*, 2013, **5**, 12804-12810.
86. A. Xu, M. Yao, G. Xu, J. Ying, W. Ma, B. Li and Y. Jin, *International journal of nanomedicine*, 2012, **7**, 3547.
87. J.-i. Jo, I. Aoki and Y. Tabata, *Journal of Controlled Release*, 2010, **142**, 465-473.
88. S. Jeong, Y.-i. Kim, H. Kang, G. Kim, M. G. Cha, H. Chang, K. O. Jung, Y.-H. Kim, B.-H. Jun and Y.-S. Lee, *Scientific reports*, 2015, **5**, 9455.
89. J. HoonáLee, *Chemical Communications*, 2010, **46**, 8615-8617.

요 약 (국문 초록)

표면 증강 라만 산란 (SERS, Surface-enhanced Raman scattering)은 분자 특이적인 신호와 좁은 선폭으로 인해 다중 측정에 유용하게 사용될 수 있다. 또한, SERS 나노프로브의 구조를 조절함으로써 새로운 기능을 부여하거나, 매우 강한 SERS 신호를 발생시키는 나노구조체를 개발할 수 있어 다양한 응용이 가능하다.

제 1장에서는 초상자성 산화철 나노입자들과 은 나노입자, 그리고 형광 실리카 층을 포함하는 자성-형광-SERS 나노프로브 (MF-SERS dot)를 합성하였다. MF-SERS dot은 초상자성과 형광을 동시에 가졌으며, 은 나노입자 층에 4-플루오로벤젠티올 (4-FBT), 4-클로로벤젠티올 (4-CBT), 4-브로모벤젠티올 (4-BBT), 3,4-디클로로벤젠티올 (3,4-DCT) 등 네 종의 라만 표지 물질을 도입함으로써 네 종류의 각각의 강한 SERS 신호를 발생시킬 수 있었다. 또한 MF-SERS dot을 세포 내로 흡수시킨 후 외부 자기장을 이용하여 효과적으로 세포 분리를 할 수 있었으며, 세포 내에 흡수된 MF-SERS dot으로부

터 SERS 신호와 형광 신호 모두를 동시 측정가능하였다. 또한, CD44 항원에 선택적으로 결합할 수 있는 CD44 항체를 MF-SERS dot 표면에 도입할 경우, CD44 항원이 발현되어있는 MDA-MB-231 세포에 효과적으로 결합되었고, 이같은 특성들을 이용하여 세포의 다중 검출과 분리에 MF-SERS dot이 효과적으로 이용될 수 있음을 확인하였다.

제 2장에서는 기하학적 패턴 및 SERS 신호를 갖는 직경 5 μm, 두께 1 μm의 디스크 형태 실리카 물질을 기반으로 한 마이크로-인코더를 이용하여 펩토이드 서열을 인코딩하였다. 마이크로-인코더는 1 μm 크기의 구멍들이 존재하도록 하였고, 표면에 은 나노입자를 코팅하고 라만 표지 물질들(4-FBT, 4-CBT, 4-BBT)을 처리함으로써 각각의 SERS 신호를 발생시킬 수 있었다. 마이크로-인코더 내부의 구멍의 개수는 펩토이드의 서열을, SERS 신호는 펩토이드 잔기의 종류를 각각 코딩하도록 하였고, 100 μm 크기의 고분자 비드 위에서 펩토이드 서열을 합성할 때마다 고분자 비드 표면에 마이크로-인코더를 흡착시켜 인코딩할 수 있도록 하였다. 이때 투입된 마이크로-인코

더의 양을 증가시킬수록 비드 표면에 흡착되는 마이크로-인코더의 양이 증가하였으며, 펩토이드 합성 과정 중에 비드 표면에 마이크로-인코더를 도입할 경우 처리해 준 양 대비 약 10%의 마이크로-인코더가 비드 표면에 남아 있음을 확인하였다. 또한 펩토이드 합성을 위해 브로모아세트산과 아민을 번갈아 반응시킬 때 마이크로-인코더가 비드 표면에 안정적으로 존재하면서도 펩토이드 합성 반응이 효율적으로 진행될 수 있도록 반응물의 양을 각각 비드의 아민 기능기 대비 10 당량으로 최적화하였다. 모델 반응으로 스트렙타아비딘과 작용할 수 있는 펩토이드 서열로써, 2-메톡시에틸아민 (N_{mea}), *N*-(3-아미노프로필)-2-피롤리돈 (N_{app}), 1-나프틸메틸아민 (N_{nap}), 피페로닐아민 (N_{pip}), 이소부틸아민 (N_{leu})을 순서대로 반응시키면서 마지막 세 서열인 N_{nap}, N_{pip}, N_{leu}에 대해 인코딩을 진행하였다. 스타렙타아비딘과 작용한 비드로부터 최종 펩토이드 서열의 정보는 표면에 위치한 마이크로-인코더의 기하학적 패턴과 SERS 신호로부터 확인할 수 있었다. 이로부터 마이크로-인코더가 펩토이드 뿐만 아니라 작은 분자량의 유가분자 리간드 화합물 스크리닝에도 유용하

게 사용될 수 있음을 확인하였다.

주요어 : 표면 증강 라만 산란, 다기능성 나노입자, 초상자성 나노입자, 세포 분리, 다중 검출, 생체 영상화, 펩토이드, 광학적 인코딩, 펩토이드 인코딩, 그래픽 인코딩, 리간드 스크리닝

학 번 : 2013-20997